lucas.thiel@unibas.ch

Spin Coherence in Nitrogen-Vacancy Centers

Master Thesis at University of Basel

Lucas Thiel

June 23, 2014

Supervisor: Patrick Maletinksy

Contents

1 Introduction

The name diamond derives from the ancient Greek word *adamas* meaning invincible. In its history diamond has already proven its invincibility in many disciplines. It is the hardest naturally occurring material on earth, posses a higher thermal conductivity than any other solid substance and the next exceptional property is currently investigated - the capability of long coherence [1].

Just like a classical bit in a classical computer, a quantum bit in a quantum computer loses its information over time. The timescale over which this happens is characterized by the coherence time. In order for a quantum computer to work at room temperature, this coherence time needs to exceed a critical value which is not the case for most of the quantum systems currently investigated [2, 3]. In contrast, single spin defects in diamond, specially the Nitrogen-Vacancy center (NV-center), exhibit coherence time up to 2 ms at room temperature which makes it a very attractive quantum system for quantum computing at room temperature. The Nitrogen-Vacancy center is one of numerous color centers in diamond but it features unprecedented properties. It is a stable single-photon source at room temperature [4], a robust temperature sensor on the nanometer-scale [5] and can sense electric fields with high sensitivity [6], which can be harnessed to sense individual charges.

Long coherence times are not only useful in the field of quantum computing but also for magnetic sensing applications. As we will see in chapter 3 the magnetic field sensitivity scales as the inverse of the square root of the coherence time, i.e. a long coherence time results in a high field sensitivity. In the recent year magnetic field sensors have had a huge impact on a broad spectrum of scientific areas from chemistry over physics to medicine. One of the most famous magnetic imaging tools is magnetic resonance imaging (MRI) which is capable of creating detailed images of the human body and is thus helping to diagnose many diseases and supporting fundamental research. There has been much effort to develop new magnetic sensing tools with constantly improving sensitivity and resolution like magnetic force microscopy [7], scanning Hall probes [8] and superconducting interference devices [9]. But only the NV-center in diamond allows for high resolution and high sensitivity magnetometry at room temperature and at atmosphere.

Exceptional purity and strong bonds of the diamond lattice as well as low spin-orbit coupling [10] makes the NV-center very stable against environmental

disturbances. As a consequence the NV-center yields the longest coherence time of a solid state electron spin at room temperature [1], which enables a high magnetic field sensitivity. Moreover, the NV-center is an atomic-sized point defects that can be localized extremely close (within few nanometer) to a magnetic sample providing nanometric spatial resolution [11]. These two properties render the NV-center a perfect candidate for magnetic field sensors and allow for probing physical and biological phenomena that were inaccessible to previous technologies.

The structure of this thesis is as follows: Chapter 2 is dedicated to the NV-center, its spin and optical properties as well as its host material diamond. Chapter 3 presents the principle of DC and AC magnetometry. There, the importance of long coherence for magnetometry is pointed out. However, as we fabricate scanning probes that we use for magnetometry, the coherence time of the NVs decreases by an order of magnitude due to the creation of ubiquitous electronic spins on the surface of diamond. The discovery of those surface spins is presented in chapter 4. The following two chapters will introduce two different approaches to maintain the rather long coherence time of NVs in bulk diamond. Chapter 5 presents an approach to pin the surface spins and inhibit their decoherence on the NV-center. Chapter 6 will deal with an alternative fabrication of scanning probes that prevent the creation of the surface spins a priori. Finally chapter 7 presents results on detecting spin labels on the surface of the diamond. In addition it was tested if the surface spins can be exploited for spin amplified magnetic field sensing [12].

This work was performed at the University of Harvard in the group of Amir Yacoby.

2 NV-centers in diamond

The Nitrogen-Vacancy center has been studied for several decades [13, 14]. It consists of a substitution nitrogen atom next to a vacancy in the diamond lattice and is an optically active point defect. Its ground state is a spin-triplet (S=1) and its spin state can be optically initialized, coherently manipulated and optically read out.

As already mentioned the NV-center has exceptional properties (atomic size and long coherence time) even at room temperature. The NV-center owns these excellent properties to its host material - diamond. Therefore the first part of this chapter is dedicated to diamond. Then the NV-center itself will be introduced in more detail. The creation process, the electronic structure and its optical properties will be presented.

2.1 Diamond

Diamond is valued for its unprecedented hardness and heat conductivity. Owing to these properties, it is frequently used as a grinding tool or heat sink. But diamond is also one of the most expensive gemstones due to its sparkling beauty when cut.

From a physical point of view diamond consists out of sp^3-hybridized, covalently bound carbon atoms. Diamond forms a face-centered cubic with two bases. The nearest neighbor distance is 1.44 Å and the lattice constant 3.57 Å [15]. It has a large bandgap of 5.48 eV ($\widehat{=}$ 226 nm) [15] which makes it transparent to light from the ultraviolet to the infrared. This has potential applications in light-emitting diodes and high-power electronics.

The hardness provided by the covalent bonds and the tightness of the diamond lattice makes it especially difficult for impurities to enter the diamond. The most abundant impurities are boron and nitrogen because their atom size is comparable to the one of carbon. This makes diamond a rather spin-free host which favors long coherence times. In most quantum systems, magnetic field fluctuations from the dipolar field of nuclear spins limit the coherence time as in GaAs [16]. However, the most abundant nuclear spins in diamond, ^{13}C ($I = 1/2$) represents only 1.1 % of all carbons in diamond.

In addition to this low spin concentration in diamond the Debye temperature of diamond is very high (1860 K [17]) due to the stiffness of the covalent bonds and spin-orbit is low due to the light mass of Carbon. Thus phonon excitations at

room temperature are highly suppressed which again favors long coherence and long spin-lattice relaxation times.
Most diamonds in research are artificial diamonds. Similar to the creation of natural diamonds, artificial diamonds can be grown from a seed crystal under high-pressure and high-temperature (HPHT)[18]. Although this is a widely used method in industrial applications which makes it a rather cheap process, chemical vapor deposited (CVD) grown diamonds are preferred for NV applications. Here a seed diamond is put into a plasma chamber and certain gasses containing carbon are constantly streamed onto the diamond, which reacts with a hydrogen plasma. This diamond growth occurs at lower temperature and pressure compared to the HPHT method. A big advantage over the HPHT method is that one can introduce impurities in a controlled way. For instance, when introducing Nitrogen for a tiny amount of time a so called delta-doped layer of NVs can be produced that are well confined in one layer [19]. Furthermore since the amount of impurities in a CVD grown diamond can be controlled, it is possible to produce diamonds with a super low concentration of paramagnetic impurities. This also led to the development of isotropically engineered diamonds. When using only gases containing the spin-free carbon isotope ^{12}C the amount of nuclear spins can be depleted to 0.01 % [1, 20].

2.2 Nitrogen-Vacancy Center

The Nitrogen-Vacancy center consists of two naturally occurring defects in diamond - a vacancy and a nitrogen atom. A single vacancy on its own is an electronic paramagnetic impurity and optically active. A diamond containing many vacancies appears greenish [21]. Since the size of the nitrogen atom is comparable to the one of carbon, nitrogen is one of the most abundant impurities in diamond. Nitrogen has one additional electron compared to carbon which makes it a paramagnetic impurity as well. Nitrogen gives the diamond a yellow color. [22].
As the name already indicates the Nitrogen-Vacancy center is made out of both these defects - a vacancy and nitrogen. Carbon atoms from two adjacent lattice sites are replaced by a nitrogen and a vacancy as depicted in Fig. 1. Its symmetry axis is orientated along one of four possible crystallographic directions. There are two charge states of the NV-center namely NV^0 and NV^-. Since the negatively charged state is much more abundant than the neutrally charged state and since

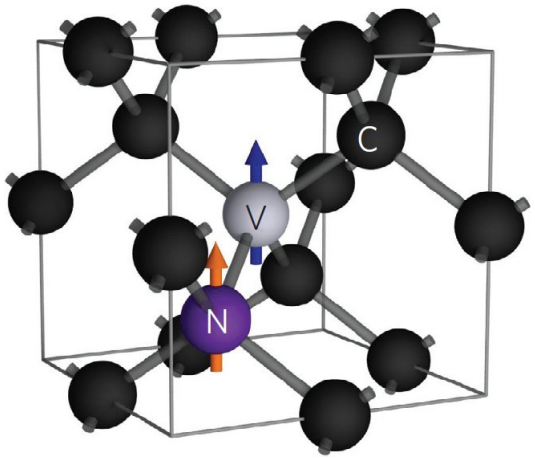

Figure 1: *Diamond lattice exhibiting a single Nitrogen-Vacancy center. Diamond consists of covalently bound carbon atoms forming a face-centered cubic lattice. The carbon atoms are coloured black. When an NV-center is formed, two carbons are replaced by a nitrogen (purple) and a vacancy (gray) having a S=1 spin.*

only the negatively charged state is appropriate for magnetometry, this work will focus on the negatively charged NV^- and we will refer to it as the NV-center.

The NV-center is strongly optically active and has an electron spin S = 1. Its ground state is a spin triplet with a zero field splitting of 2.87 GHz. An NV can be identified either optically or with electron spin resonance experiments [23].
NVs are formed naturally in diamond but can be artificially produced by implanting nitrogen into diamond or by producing vacancies by irradiation of high energy electrons. While nitrogen atoms stay at their lattice site, at temperatures higher than 600 °C the vacancies get mobile and start to diffuse through the diamond until they get trapped by a nitrogen impurity. The nitrogen to NV conversion is less than 50% in bulk [24] with decreasing tendency for shallow Nitrogen-Vacancy centers due to decreasing amount of vacancies and higher probability for the vacancies to heal out the diamond during annealing [25].

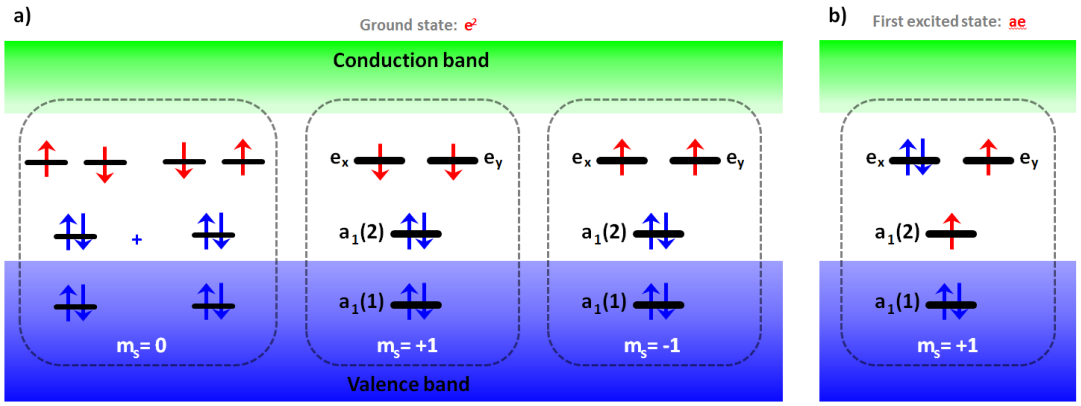

Figure 2: *Ground and first excited state of the NV triplet.* ***(a)*** *The negatively charged NV-center has six electrons. In the ground state those six electrons are distributed according to Hund's rule to give the lowest energy with two holes in the e-orbitals - e^2 state. For clarity the spins giving spin projection of $m_s = 0, \pm 1$ are colored red.* ***(b)*** *When exciting the system one electron from an A_1-orbit reaches the higher E-orbit - ea state. As for the ground state there are also three spin-subleveles with $m_s = 0, \pm 1$ for the excited state, but only the $m_s = 1$ state is drawn here.*

2.3 Electronic Structure

The electronic properties of the NV-center are governed by the symmetry of its structure. As can be seen in Fig. 1 the NV center has a C_{3v} symmetry (identity, rotation around $2\pi/3$, reflection along the three planes defined by the NV axis and the neighboring carbon atom).

The negatively charged NV-center has a total of six electrons forming a spin-triplet. The three dangling bonds from three carbons contribute three electrons. The nitrogen contributes the two electrons from its lone pair and there is one additional electron originating from nearby substitutional nitrogen in the bulk or from the surface. An ideal N to NV conversion is around 50% such that half the Nitrogen atoms form an NV-center and the second half donates one electron to the NVs.

Group theoretical calculations yield an electronic level diagram exhibiting four orbits, but only six electrons are associated with the NV-center resulting in two holes as depicted in Fig. 2. Often it is easier to theoretically describe the NV-center in terms of the two holes [26] rather than six electrons [27]. The lowest two orbitals are of A_1 symmetry while the two highest degenerate states are of E symmetry. The ground state of the NV-center is a triplet state and has two holes, one in each of the highest orbitals. There are three ground states with spin projection $m_s = 0$ and $m_s = \pm 1$. The ground state in terms of holes is called e^2. The orbitals are

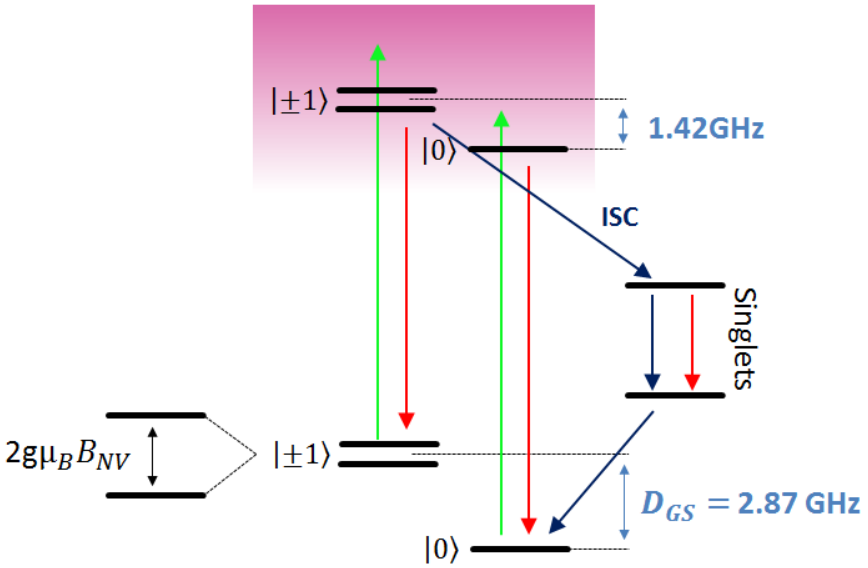

Figure 3: *Electronic structure of the NV-center at room temperature. Both the ground and the excited triplet states are split due to the dipolar field of the spins. A magnetic field along the NV axis leads to a splitting of the $m_s = \pm 1$ states. The excited state are separated from the ground state by 1.945 eV (637 nm). Green lines indicate green laser excitation into the phonon sideband. Red lines are emissions into the phonon sidebands. Blue lines indicate non-radiative decay mainly from the $m_s = \pm 1$ excited to the metastable singlet state and back to the $m_s = 0$ ground state. Continuous illumination leads to initialization into the $m_s = 0$ state due to intersystem crossing (ISC). Further $m_s = \pm 1$ population transferred to the singlet state will remain dark while $m_s = 0$ population will continuously emit photons. This leads to spin dependent fluorescence.*

antisymmetric with spin S = 1. The singlet state with symmetric orbitals is higher in energy and plays an important role for initialization and readout of the spin state as discussed later.

When a photon with energy of 1.945 eV (637 nm) or higher gets absorbed by the system, a hole gets promoted from an e-orbit to an $a_1(2)$-orbit and the system reaches the first excited state (Fig. 2b). The excited state has a hole in one of the A-orbits and the E-orbit and is therefore called ea. An overview of the electronic level structure of the NV is depicted in Fig. 3. As already discussed the NV-center has three triplet states in the ground state with $m_s = 0$ and $m_s = \pm 1$. The $m_s = \pm 1$ states are split in energy from the $m_s = 0$ state due to spin-spin interaction by $D_{gs} = 2.87$ GHz at zero field. This parameter is temperature sensitive [5]. Due to their magnetic moment, only the $m_s = \pm 1$ states are sensitive to magnetic fields and get shifted by the Zeeman energy $\Delta\omega = m_s \gamma B_{||}$ with the gyromagnetic ratio $\gamma = g\mu_B/h = 2.8$ MHz/G. m_s is the quantum number for spin projections along the NV axis. The NV-center is, to first order ($B_\perp \ll D$), only

sensitive to magnetic fields parallel to the NV axis. At zero field, the $m_s = \pm 1$ states can also be split by strain which is characterized by the parameter E (not shown in the image) [28].
Optical transitions between the ground and excited states feature a zero-phonon line (ZPL) at 637 nm with a broad phonon sideband that stretches from 637 nm to 750 nm [29]. These optical transitions are highly spin-preserving ($\Delta m_s = 0$). However, there is an alternative relaxation path involving the singlet ground state of the NV (see Fig. 3). The singlet states allow for intersystem crossing (ISC), which are spin selective, i.e. the probability to shelf into the singlets from the $m_s = \pm 1$ states is much higher than from the $m_s = 0$ state [30]. Once in the metastable singlet state, the population decays preferentially to the $m_s = 0$ state. Therefore population from the $m_s = 0$ state will always cycle between $m_s = 0$ ground and excited state upon excitation, while population from the $m_s = \pm 1$ will eventually shelve into the metastable singlet state and relax into the $m_s = 0$ state. Continuous illumination of the NV-center will therefore optically initialize the NV-center into the $m_s = 0$ state with high fidelity.
Furthermore, since the ISC does not involve the emission of a photon and the lifetime of the singlet state is much longer ($\approx$ 300 ns) than the lifetime of the excited states ($\approx$ 20 ns) [29], $m_s = \pm 1$ population gets stuck for a while and the fluorescence count rate for the $m_s = \pm 1$ population is much lower than for the $m_s = 0$ population. This spin dependent florescence rate enables optical spin readout. Hence, the NV center can be optically initialized as well as optically readout as illustrated in the next subsection.

2.4 Electron spin resonance

By means of optical initialization and spin dependent fluorescence it is possible to directly probe the ground state of the NV-center. In an electron spin resonance (ESR) experiment the NV is spin-polarized into the $m_s = 0$ state under continuous illumination of green laser light. Additionally a time-varying magnetic field with frequency ω is applied. If the frequency is swept and is resonant with the $m_s = 0$ to $m_s = \pm 1$ transition, population is transferred to the $m_s = \pm 1$ states which leads to a reduction in fluorescence as illustrated in Fig 4 (lowest curve).
As a next step, a static magnetic field can be applied that splits the $m_s = \pm 1$ according to the Zeeman-splitting

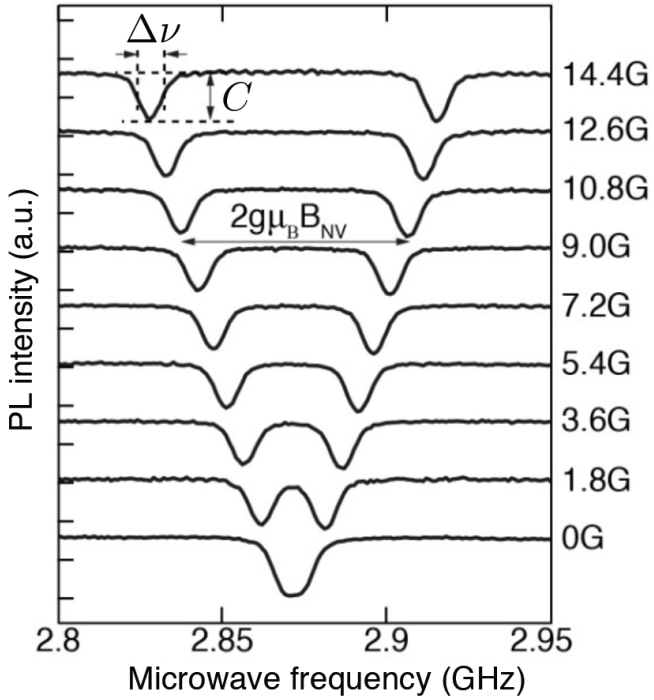

Figure 4: *Electron Spin Resonance of the NV-center. The NV-center is continuously illuminated with green laser light while the frequency of an applied magnetic field is swept (horizontal axis). If the frequency of the magnetic field is resonant with one of the ground state transitions, population is transferred to the darker $m_s = \pm 1$ and a dip in fluorescence (left vertical axis) is observed (lowest curve). Applying a static magnetic field along the NV-axis (right vertical axis) induces Zeeman-splitting of the $m_s = \pm 1$ states and two dips are visible. Image taken from [31].*

$$\Delta\omega = \frac{g\mu_B B_{NV}}{h} \tag{1}$$

where $\Delta\omega$ is the shift in resonance frequency, g the g-factor (≈ 2) of the NV-center, μ_B the Bohr magneton and B_{NV} the magnetic field along the NV axis. This leads to two transitions within the ground state: $m_s = 0$ to $m_s = -1$ and $m_s = 0$ to $m_s = +1$. Both transitions are observable in an ESR experiment. The splitting between the two resonance dips scales linearly with the applied magnetic field. The contrast C of the dips is fixed by the branching ratio to the singlet states at low optical and RF power. The non-zero width of the dips is given by inhomogeneities in the environment that produce magnetic fields which again lead to a jitter of the resonance frequency. The FWHM ($\Delta\nu$) is limited by the inverse of the inhomogeneous dephasing time T_2^*.

3 Magnetometry

One of the most promising applications of the NV-center is magnetometry with high magnetic field sensitivity and high spatial resolution. This application could have an immense impact in a wide range of fields from fundamental physics to material science, chemistry and data storage, life science and medical science. Almost all molecules and physical systems possess a magnetic trace and many approaches to magnetometry have been developed to detect large fields with high resolution and small fields with low resolution as depicted in Fig. 5.

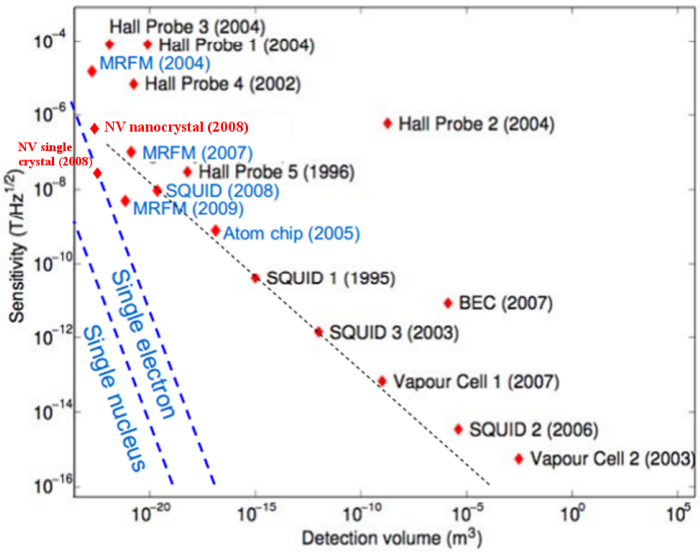

Figure 5: *Magnetic field sensitivity versus detection volume. The dashed blue lines indicate the dipole magnetic fields of a single electron and a single proton. Image taken from [32].*

There are many imaging schemes with good sensitivity and high resolution like scanning Hall probe microscopy [8], superconducting interference devices (SQUIDS) [9] or magnetic force microscopy [7]. But all of these methods can only be operated at cryogenic temperatures or under vacuum. There is no adequate magnetometer at ambient conditions.

As mentioned in the previous section, the Nitrogen-Vacancy center has exceptional physical properties that renders the NV-center a perfect magnetometer at ambient conditions. Since the NV-center is a point defect, its wave function is localized on a nanometer length scale, which enables spatial resolution below the diffraction limit of light. Furthermore the NV-center features long coherence time at room temperature yielding high magnetic sensitivity as discussed in the next section.

3.1 Sensitivity to a DC magnetic field

The easiest way to detect a DC magnetic field is to measure the Zeeman shift of an electron spin resonance curve as discussed in section 2.4. A static magnetic field induces a frequency shift of 2.8 MHz/Gauss. The magnetic field sensitivity is given by the maximum slope of the resonance dips and is inversely proportional to the dephasing time T_2^* as derived in the following part.

The intensity profile of an resonant ESR dip can be fitted to [33]

$$I(\nu) = R\left[1 - C \cdot F\left(\frac{\nu - \nu_o}{\Delta\nu}\right)\right] \tag{2}$$

where R is the rate of detected photons, C the ESR contrast, F the lineshape of the dip and $\Delta\nu$ the FWHM. The sensitivity is limited by the noise associated with the fluorescence photons called photon shot noise δI. Hence, the smallest resolvable field change i.e. frequency change $\delta\nu$ for a signal-to-noise ratio of 1 is

$$\delta\nu \cdot \frac{\partial I}{\partial \nu} = \delta I \tag{3}$$

where $\partial I/\partial\nu$ is the slope of the ESR resonance dip. During a time τ the number of collected photons can be approximated by $I\tau = R\tau$. The corresponding photon shot noise is $\delta I = \sqrt{R}$. The measurement is most sensitive at the point of highest slope $max\left|\frac{\partial I}{\partial \nu}\right|$ which is given by $0.77\frac{CR}{\Delta\nu}$ for a Lorentzian dip. The sensitivity then is given by

$$\eta_{ESR} = \delta B\sqrt{\tau} = \frac{\delta\nu}{\gamma}\sqrt{\tau} = \frac{\delta I}{\gamma \cdot max\left|\frac{\partial I}{\partial \nu}\right|}\sqrt{\tau} = \frac{\sqrt{R\tau}}{\gamma\left(0.77\frac{CR}{\Delta\nu}\right)} = 0.77\frac{h}{g\mu_B}\frac{\Delta\nu\sqrt{\tau}}{C\sqrt{R}} \tag{4}$$

The sensitivity is proportional to the the linewidth $\Delta\nu$ and inversely proportional to the contrast and the square root of the count rate. These parameter are not completely independent of each other. The contrast C can be increased by increasing the microwave power. However, this leads to power broadening of the resonance ESR dip and a larger linewidth $\Delta\nu$. The linewidth on the other hand can be decreased by lowering the power of the excitation laser at the expense of a decreasing count rate. This can be mitigated using a pulsed ESR version. There the microwave and the green laser will be separated in time. An alternative way to measure a DC field that avoids power broadening is by applying a Ramsey sequence. The pulse sequence is depicted in Fig. 6. In the Bloch sphere picture (see Fig. 6b) the north pole represents the $m_s = 0$ state and the south pole the $m_s = 1$

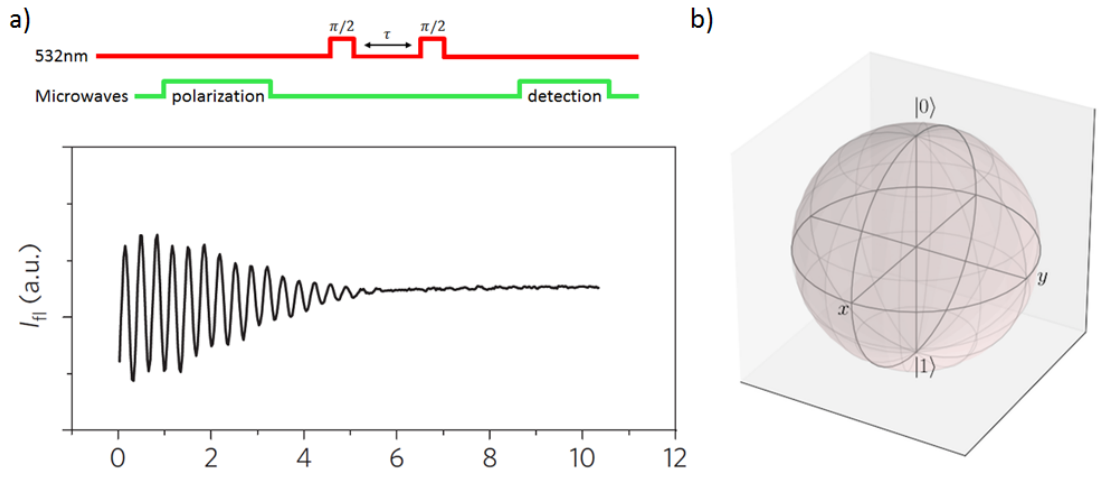

Figure 6: ***(a)*** *Ramsey sequence of an NV. Top: Ramsey sequence. Bottom: Population oscillation with a frequency proportional to the applied static magnetic field. Image taken from [1].* ***(b)*** *Bloch-sphere. The north pole is represented by the $m_s = 0$ state and the south pole by $m_s = 1$, respectively.*

state[1]. A green laser pulse initializes the NV into the $m_s = 0$ state. The first mircowave pulse applied then is resonant with the $m_s = 0$ to $m_s = 1$ transition and will rotate the spin 90° into the equator plane. This pulse is called a $\pi/2$ pulse. There, the spin acquires a phase $\phi = 2\pi\gamma\tau B$ from a given DC magnetic field for time τ. The second $\pi/2$ pulse rotates the spin back onto its quantization axis thereby converting the phase ϕ into a population difference, which can be read out by a subsequent green laser pulse.

Here the spin manipulation, the phase accumulation and the read out is separated in time to avoid power broadening. The phase increases proportionally to τ. From the measured oscillation frequency the magnetic field B can be extracted. The calculation for the sensitivity yields the same results as for ESR. The lower limit of the linewidth $\Delta\nu$ is the dephasing time T_2^* with maximal measurement time $\tau = T_2^*$ such that the best DC sensitivity is

$$\eta_{ESR} \approx \frac{h}{g\nu_B} \frac{1}{C\sqrt{R \cdot T_2^*}} \tag{5}$$

T_2^* lies in the range of 0.1 us to 100 us in isotropically purified diamonds with sensitvities from 1.5 uT/$\sqrt{Hz}$ to 50 nT/$\sqrt{Hz}$ [1].

[1]In an applied magnetic field the NV-center can be considered as a simple two level system.

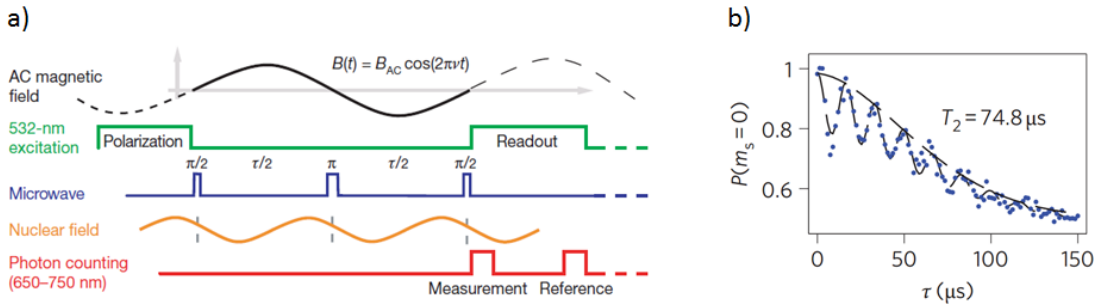

Figure 7: *Principle of AC magnetometry using a spin-echo sequence.* ***(a)*** *The NV is optically polarized into the $m_s = 0$ state. It is then prepared into a superposition state, where it starts to precess. After refocusing, it evolves freely for a second period of $\tau/2$. Eventually it is projected back into the $\{|0\rangle, |1\rangle\}$ manifold. A green laser pulse reads out the spin state via spin dependent florescence. The NV is most sensitive to fields with frequency $1/\tau$. Image taken from [35].* ***(b)*** *Typical spin-echo measurement for a single NV-center. The collapses and revivals are stemming from interactions with the ^{13}C nuclear spin bath [36]. The signal was fitted to an exponentially decaying envelope function, yielding a coherence time of 74.8 us. Image taken from [11].*

3.2 Sensitivity to an AC magnetic field

The sensitivity can be further increased by decoupling the NV from its nuclear spin bath. The simplest sequence to achieve decoupling adds a π-pulse in the middle of the Ramsey sequence: $\pi/2 - \tau/2 - \pi - \tau'/2 - \pi/2$ as can be seen in Fig. 7. This sequence is called either spin-echo or Hahn-echo [34]. After the first $\pi/2$-pulse the NV is a superposition state $\frac{1}{\sqrt{2}}(|0\rangle + i\,|1\rangle)$. Due to Larmor precession, the NV collects a phase $\frac{1}{\sqrt{2}}(|0\rangle + ie^{i\phi}\,|1\rangle)$ with $\phi = \int_o^{\tau/2} g\mu_B B(t)/\hbar$. The π pulse rotates the spin around an axis perpendicular to the NV axis such that the NV is in the state $\frac{1}{\sqrt{2}}(-ie^{i\phi}\,|0\rangle + i\,|1\rangle)$. Then the NV collects another phase ϕ' during the second evolution time $\tau'/2$ giving $\frac{1}{\sqrt{2}}(-ie^{i\phi}\,|0\rangle + ie^{i\phi'}\,|1\rangle)$. For $\tau = \tau'$ the phase factors are the same ($\phi = \phi'$) in static magnetic fields and factor out, such that a final $\pi/2$-pulse rotates the NV back into the $m_s = 0$ state. Noise with components on a time scale much longer than $\tau/2$ are filtered out and the dephasing time is increased from T_2^* to the coherence time T_2.

$$\eta_{AC} \approx \frac{h}{g\nu_B} \frac{1}{C\sqrt{R \cdot T_2}} \tag{6}$$

T_2 lies in a range from 1 us to 2 ms and the sensitivity from 500 nT/$\sqrt{Hz}$ to 10 nT/$\sqrt{Hz}$ [1].

3.3 Discussion

In general the sensitivity for either DC or AC magnetometry is proportional to

$$\eta \approx \frac{1}{C\sqrt{R \cdot \tau}} \tag{7}$$

where C is the resonance contrast, R the number of photons collected per measurement and τ the measurement time. The contrast depends on the ISC rate of the NV electronic structure and is therefore fixed for a given NV. The photon collection rate is limited by the NV's collection efficiency (see section 3.3.1) and the measurement time is limited by the coherence time (see section 3.3.2).

3.3.1 Collection efficiency

For most confocal setups, the collection efficiency is on the order of 1%. This is mainly limited by the high refractive index of diamond (n=2.4), which leads to total internal reflection. Hence, most of the photons emitted by the NV get reflected at the diamond-air interface and get trapped within the diamond itself as depicted in Fig. 8b).

To improve collection efficiency one could either position detectors around the diamond sample to collect photons leaving the diamond through its side [37] or to avoid refraction. One possibility is to use nano-diamonds with a size smaller than the wavelength of emission light [38] at the expense of low coherence time, since the quality of diamond crystals is rather poor. Additionally the NV-center is closer to the surface and the defects and impurities associated with it. Another possibility is to place a solid immersion lens (SIL) on top of the diamond [39]. Owing to the high refractive index (N = 3.3 for a GaP SIL) and its geometry, the SIL not only changes the refraction but can also increase the collection angle. The collection efficiency can be increased further by thinning down the diamond and thereby realizing a dielectric antenna.

Finally the collection efficiency can be increased by coupling the NV-center and the optical modes of a nanowire (Fig. 8a). According to a simulation a coupling of more than 80% of the emitted photons to the nanowire mode has been predicted and could be efficiently collected with an high NA objective [40, 41].

The number of collected photons observed was as high as $3 \cdot 10^5$ CPS in a (100)-orientated diamond nanopillar, while for a shallow NV-center in bulk the number of counts corresponds only to a couple 10 kCPS. Only recently the growth

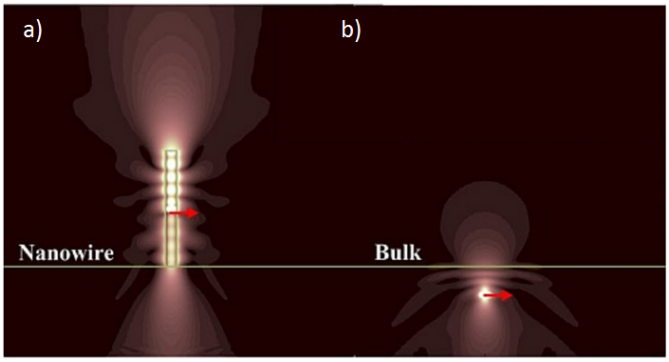

Figure 8: *Finite-difference time-domain simulation of the field profile of the E-field's radial component in a 2 um long, 200 nm in diameter diamond nanowire (b) and bulk diamond (a). Image taken from [40].*

of (111)-orientated diamond became possible and featured NV-centers with good physical quality (normal excited state lifetime and long coherence time) [42]. Saturated fluorescence count rates from NVs in pillars in this (111)-orientated diamond are reported to be in excess of 10^6 CPS [43].

3.3.2 Measurement time

In case of the DC magnetometry, the measurement time τ is limited by the dephasing time T_2^*. Dephasing occurs due to inhomogeneities in the environment. These inhomogeneities produce slow, time varying magnetic fields that are hyperfine coupled to the NV-center, which shift the resonance frequency of the spin transition and, hence, lead to an increased linewidth in an ESR experiment. In a standard bulk diamond sample with 1.1% abundance of ^{13}C and less than 15 ppb nitrogen, the main dephasing originates from the dynamics of the surrounding nuclear spin bath. Typical time scales for T_2^* are around 1 us [44]. In samples with a nitrogen concentration of more than 15 ppb the electronic spins of substitutional nitrogen contribute to the dephasing as well [45]. In isotropically engineered bulk diamond samples, T_2^* up to 100 us were observed [1].
In the case of the AC magnetometry, the measurement time τ is limited by the coherence time T_2. The coherence time is a characteristic time for homogenous spin dephasing for a given decoupling sequence. Again the main decoherence source are nuclear spins of the ^{13}C bath [36] as seen in Fig. 7 b). However, whenever the free precession time equals a multiple of the Larmor frequency of those ^{13}C, $\tau = 2n/\gamma_{^{13}C}B$ with $\gamma_{^{13}C} = 1.071$ kHz/G, the phase collected during the two evolution times exactly cancels and coherence is recovered. This is the origin of the collapses and revivals in a spin-echo measurement. The actual coherence time T_2 is given by the decaying envelope function. The

coherence time in bulk samples where ^{13}C is the dominant source is around 300 us.

The ultimate limit of the coherence time is given by the spin-lattice relaxation time ($T_2 = 2\ T_1$ [46]). Interactions with phonons inside the crystal lead to spin-flips of the NV spin until the population arrives at a thermally mixed state. T_1 is highly temperature sensitive. Since the diamond crystal has strong, covalent bonds and light atoms, phonons are highly suppressed at room temperature resulting in $T_1 \approx 6$ ms [1].

In this thesis I mainly concentrate on T_2 of NV-centers located on top of the previously introduced nanopillar. These nanopillars can be held in a monolithic scanning device as depicted in Fig. 9c) and can be used to probe magnetic samples with high resolution [11].
This scanning AFM tip features robustness, waveguiding and isolation of a single NV-center inside a 200 nm diameter pillar. The NV-center is extremely shallow ($\approx$ 15 nm) in order to decrease the distance between the sensor and the sample. Hence, spatial resolution can be pushed to the range of few tens of nanometers. However, there is an important limiting factor with the fabrication of such devices. One of the beloved features of NV-centers in diamond, namely the long spin coherence time, that provides high field sensitvity, is reduced from a few tens of us[2] to below 5 us as illustrated in Fig. 9. The samples under considerations are CVD grown (100)-orientated electric grade diamonds (Element 6) with ^{14}N implanted with 6 keV at a density of $3 \cdot 10^{11}/\text{cm}^2$ (one NV every 200 nm at 1% N to NV conversion rate). The diamonds were annealed for 2 hours at 800 °C in vacuum and the nominal depth of the formed NVs according to SRIM[3] calculations (Stopping and Range of Ions in Matter) is approximately 15 ± 3 nm below the surface [48]. Before etching pillars, the coherence time on the shallow bulk NVs are around $20 - 30$ us (Fig. 9 b). But after our etch process the T_2 of almost all pillars decay dramatically and consistently over many samples by one order of magnitude to around $1 - 4$ us (Fig. 9d).

[2]Typical coherence time for shallow NVs ($<$ 25 nm below the surface) are $\approx$ 50 us in contrast to ultralong coherence time (2 ms) for NVs in bulk.

[3]SRIM calculations do not take account of the crystal structure of diamond. Therefore a few NV-centers might be deeper due to ion channeling during implantation [47].

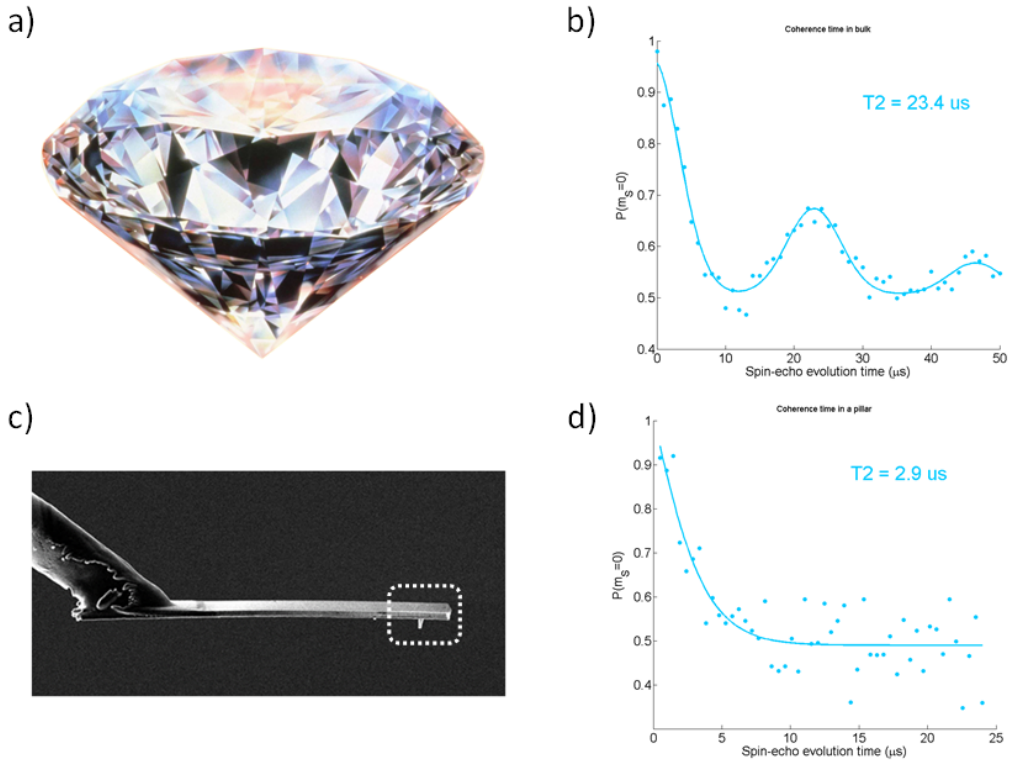

Figure 9: ***(a)***, ***(b)*** *Typical coherence time of a shallow NV in an unpatterned CVD grown diamond.* ***(c)*** *SEM image of monolithic NV AFM tip glued to a quartz rod. A single NV is positioned at the bottom end of the nanopillar in the white box.* ***(d)*** *Coherence time of an NV in an etched pillar. Compared to the bulk case, T_2 decreases by one order of magnitude.*

4 The source of decoherence

In the last chapter we have seen that etching nanowires into diamond considerably influences the coherence of the NV-centers. The origin of this phenomena was an open and outstanding question in the past. Now two independent experiments revealed that a surface bath of electronic spins are the dominant noise for NV-centers located within 25 nm below the diamond surface [49, 50].

The first experiment probed the dominant noise as a function of NV distance to the surface of diamond [49]. Thereby a change in the nature of the dominant noise spin bath was observed. While bulk NV-centers experience the noise of a 'slow bath' (correlation time $\approx$ 830 us) of fluctuating nuclear spins, NV-centers closer to the surface experience a 'faster spin bath' (correlation time $\approx$ 5 us) which is best modeled by a 2D layer of electronic surface spins.

This section, though, will deal with the methods and results of the second experi-

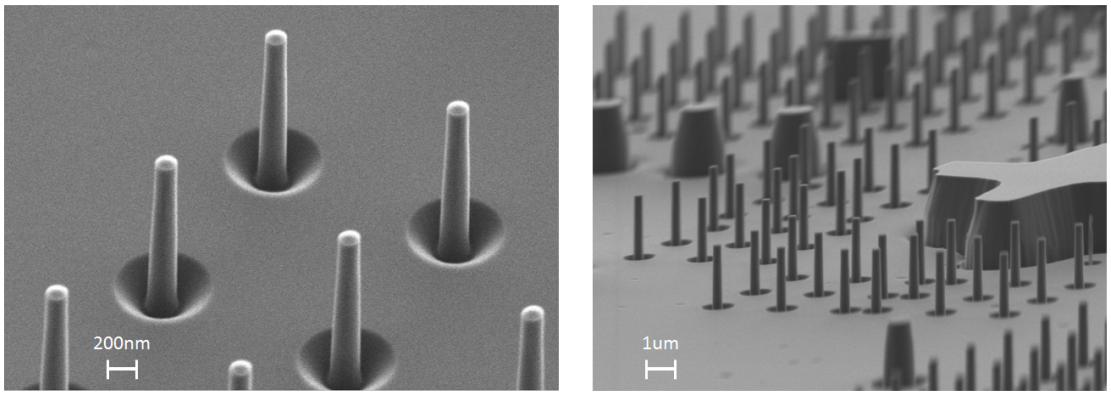

Figure 10: *Scanning electron image of nanopillars in diamond. The pillars are fabriacted by patterning cylindrical etching masks on the diamond and subsequent oxygen plamsa etch. The pillars are roughly* 200 *nm in diameter and* 1.5 *um in length.*

ment. There, magnetic resonance imaging (MRI) was employed to directly image the distribution of electronic spins on the surface [50].

4.1 Magnetic-resonance imaging of surface spins

The NV-centers used to image spins on the surface are located on the top of diamond nanopillars. The pillars isolate single NV-centers and serve as a waveguide as discussed earlier. They are fabricated by patterning the diamond with cylindrical etch-masks and subsequent etching with oxygen plasma. Scanning electron images of fabricated pillars in diamond are shown in Fig. 10.

The spins on the surface of these pillars are called dark spins as they remain dark when illuminated. The spins are statistically polarized which means they can not be detected with an NV using a standard Hahn-echo sequence since the phase $\langle \phi_{\mathrm{NV}} \rangle$ collected during the free evolution time averaged over many measurements would be zero. However, it is possible to measure the variance of the dark spins with a double electron-electron resonance (DEER) experiment [51, 52, 53]. Fig. 11 illustrates the idea behind DEER.

In contrast to a normal Hahn-echo on the NV, an additional π-pulse synchronized with the NV π-pulse is applied to the dark spins, leading to a net NV spin phase, while the field from a static spin bath refocuses and cancels out. Therefore the DEER-sequence decoheres the NV faster than the Hahn-echo sequence as depicted in Fig. 12 d). The difference between fluorescence counts of a spin-echo (greenish curves) and fluorescence counts of a DEER sequence (blueish curves) for the same evolution time is what we call DEER signal.

Performing a DEER experiment requires the knowledge of the resonance frequency

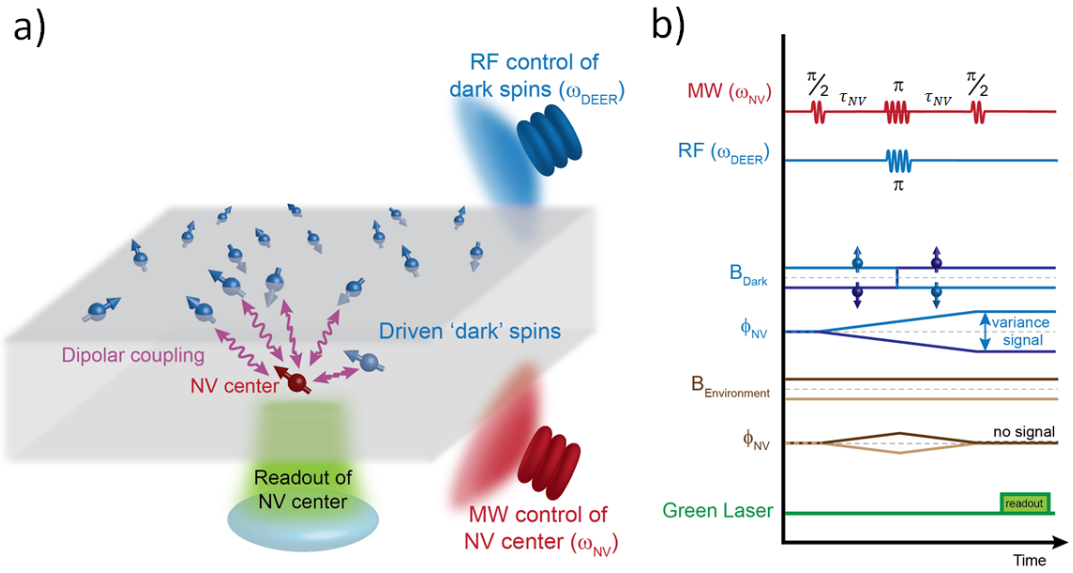

Figure 11: *Double electron-electron resonance on nearby dark spins.* ***(a)*** *A shallow NV-center (red) is embedded in diamond and surrounded by electronic dark spins (blue). The NV sits in the center of the green laser spot which is to read out the NV spin state. Two RF sources are used to independently manipulate both the NV and the dark spins.* ***(b)*** *Pulse sequences applied to the NV-center and dark spins. A $\pi/2$ microwave pulse prepares the NV in a superposition state. During a free evolution time τ_{NV} the NV collects the phase ϕ_{NV} from all dark spins. A synchronous π-pulse on the NV and on the dark spins flips them both. As a result, the phase which the NV acquires in the second evolution time due to the dark spins will not cancel out the phase from the first evolution time as it would be the case for a Hahn-echo. Finally, the NV spin state is readout with a green laser pulse via spin-dependent fluorescence.*

of the dark spins ω_0 and the microwave pulse length required to perform a π-pulse τ_π. Fig. 12 illustrates how these parameters are measured. A general DEER pulse sequence is depicted on top of Fig. 12 a) with all relevant pulse durations and frequencies labeled. In order to find ω_0 the evolution time of the NV τ_{NV} and the DEER-pulse length τ_{DEER} are fixed, while ω_{DEER} is swept. This experiment is analog to an ESR experiment on the NV and will be called DEER-ESR. If ω_{DEER} is off-resonance with the transition of the dark spins, all dark spins remain static assuming their T_1-time exceeds the evolution time τ_{NV} and no DEER-signal is observed[4]. If $\omega_{\mathrm{DEER}} = \omega_0$ dark spins will be flipped in the middle of the spin-echo sequence and the NV acquires a non-zero phase from the magnetic field of the dark spins and will decohere faster. As a result, a decrease in fluorescence of the NV is observable. Fig. 12 a) shows the outcome of this measurement. The upper two curves correspond to a spin-echo $(\pi/2_{+x} - \tau/2 - \pi_{+x} - \tau/2 - \pi/2_{+x})$ on the NV

[4]Remember that DEER-signal is the difference between fluorescence counts of a spin-echo and fluorescence counts of a DEER sequence for the same evolution time. Since no dark spins are flipped, no additional decoherence is caused.

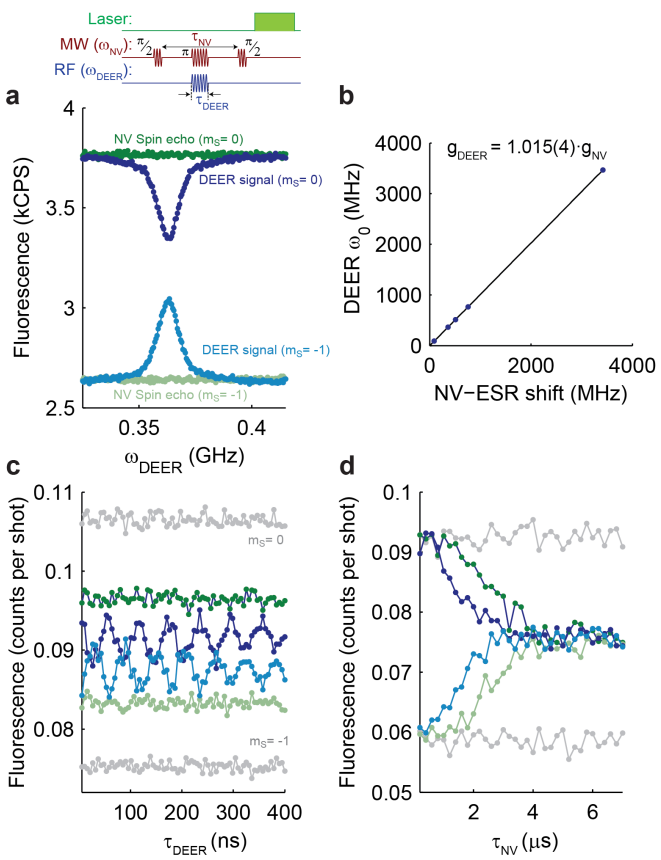

Figure 12: *DEER characterization. A general pulse sequence is depicted on top of (a) with detailed information of the sweeping parameter in the caption of each subfigure.* ***(a)*** *DEER-ESR: τ_{NV} and τ_{DEER} are fixed, while the dark spin addressing frequency ω_{DEER} is swept. On the most NVs a single resonance peak is observed. The lower two curves have a final $\pi/2_{-x}$ pulse rather than a $\pi/2_{+x}$ converting the phase difference into a population difference.* ***(b)*** *As the magnetic field strength is varied, the resonant shift of the dark spin ESR curve is in good agreement to the resonance shift of the NV-ESR curve resulting in the same g-factor of $g \approx 2$.* ***(c)*** *ω_{DEER} is fixed to resonance, while the pulse length τ_{DEER} is swept. Coherent Rabi oscillations of the dark spin can be observed. The length of a DEER π − pulse can be estimated.* ***(d)*** *ω_{DEER} is fixed on resonance and τ_{DEER} is set to a π-pulse, while the NV evolution time τ_{NV} is swept. An evolution time that maximized signal-to-noise-ratio of the DEER signal can be found. Figure taken from [50](Supplementary).*

with (dark blue) and without (dark green) π-pulse on the dark spin where (+x) is the spin rotation axis. For the lower two curves (bright blue and bright green) the projection of the NV state onto the NV $\{|0\rangle, |1\rangle\}$ manifold is achieved by a $\pi/2$ pulse around (-x) rather than around (+x) as for the upper two curves. The resonance shift of a given two level system is proportional to the g-factor times the applied magnetic field. The g-factor of the dark spins can be estimated by varying the magnetic field strength along the NV-axis and comparing the resonance shift of the NV to the dark spins. Since the shifts lie on one line (Fig. 12 b) we conclude the same g-factor for the NV and the dark spins which is ≈ 2.

Fig. 12 c) shows dark-spin Rabi-oscillations. ω_{DEER} is set to ω_0, while sweeping the pulse length τ_{DEER}. The two gray curves in the figure represent $m_s = 0$ and $m_s = 1$ state. The green curves represent the spin-echo of the NV with a fixed evolution time τ_{NV}. From the Rabi oscillations the length of a π-pulse τ_π can be estimated.

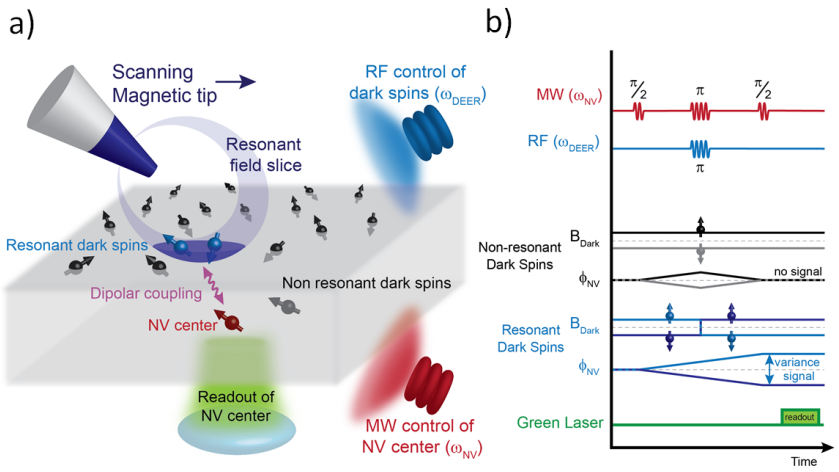

Figure 13: *NV-MRI using a scanning field gradient. Only dark spins within the resonance slice of the magnetic tip are on resonance with the driving RF field and contribute to the DEER signal. The magnetic field of dark spins being not within the resonance slice is refocused and has no effect on the NV state.*

With all the relevant parameters (ω_0 and τ_π) determined, there is only one part missing in order to create 3D images of the dark spins - a local magnetic field gradient which we produce with a scanning, magnetic tip. The applied RF frequency will be detuned from ω_0 by a small frequency shift δ_{DS} which sets all spins off-resonance. The magnetic tip has a variety of of magnetic field lines with one of them corresponding to $\delta_{\mathrm{DS}} = g\mu_B B_{\mathrm{tip}}/\hbar$. If a dark spin intersects with this magnetic field line, it will experience a Zeeman shift such that its resonance frequency becomes $(\omega_0 - \delta_{\mathrm{DS}})$. Hence, this dark spin will be on resonance with the applied RF signal while other dark spins that do not intersect this field line will be still off-resonance. The magnetic tip therefore provides a small resonant slice in which dark spins are on resonance with the applied, detuned RF field and only these dark spin will contribute to the DEER signal as depicted in Fig. 13.

The point spread function (PSF) of the dark spins describes the response of the imaging system in which all dark spins are located at the position of the NV. In case of a two dimensional scan of the magnetic tip parallel and near to the diamond surface one would expect a circular resonance ring in case of bowl-shaped field lines. Along the positions of this ring, the magnetic field line of the tip corresponds to δ_{DS} and the dark spins are on resonance, leading to decoherence on the NV and a decrease in fluorescence. A PSF for a 3D scan is displayed in Fig. 14 e). As the height of the tip is increased (positive z-direction in Fig. 14 e) the magnetic field lines will not intersect with the dark spins and the DEER signal will vanish (top layer in Fig. 14e).

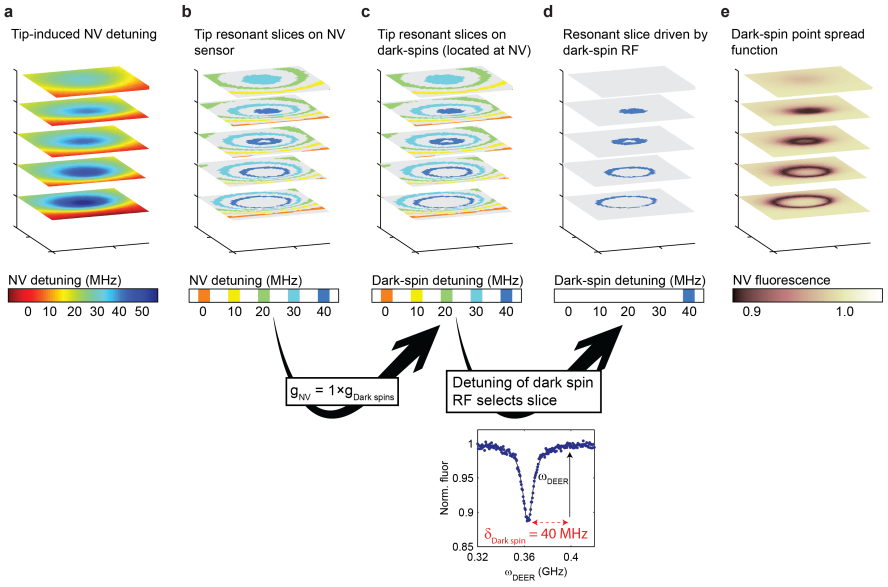

Figure 14: ***(a)*** *The detuning induced by the tip can be measured by scanning the tip over the NV-center in three dimensions while frequency-locking the driving microwave frequency to the NV spin transition frequency. (a) shows the NV detuning as a function of tip position.* ***(b)*** *This detuning can be discretized into a map of resonant slices with discrete width. The width is set to the FHWM of an ESR curve.* ***(c)*** *As disussed in Fig. 12 the dark spin g-factor is equivalent to the NV g-factor and, hence, the NV map in (b) also applies to dark spins sitting at the NV location.* ***(d)*** *While scanning the tip we selected a dark spin RF frequency which is detuned from resonance by δ_{DS}. In this example $\delta_{DS} = 40$ MHz. Hence, only the slices corresponding to the 40 MHz detuning are on resonance.* ***(e)*** *By mapping this dark-spin detuning to the full ESR spectrum, we obtain the PSF for dark spins located on the NV.*

Fig. 14 sketches how to estimate such a PSF. First the magnetic field at the position of the NV is measured as a function of tip position (Fig. 14 a). This map is equivalent to a map of resonant slices with finite width (Fig. 14 b). Up to now we have a map that displays the detuning experienced by the NV-center. This map can easily be converted to a spatial map of dark spin resonance slices by rescaling the magnitude of the detuning. Since the g-factor are the same for the NV and the dark spins the detuning stays the same (Fig. 14 c). So far we have a map for various detunings. By fixing the detuning of the applied RF to one value $\delta\omega$ we select for only one set of resonance slices. In the case of (Fig. 14 d) the detuning is chosen to be 40 MHz, which selects for every height of the tip (every plane in the sketch) the resonant slice that belongs to that detuning. As a last step the the dark spin detuning can be mapped to a ESR spectrum to obtain the width of the expected dark spin response as well as the NV fluorescence (Fig. 14 e). This is the final PSF for the dark spins. To sum up, if the tip is at the position of the blue circles indicated in (Fig. 14 d), dark spins located right on the NV will be on

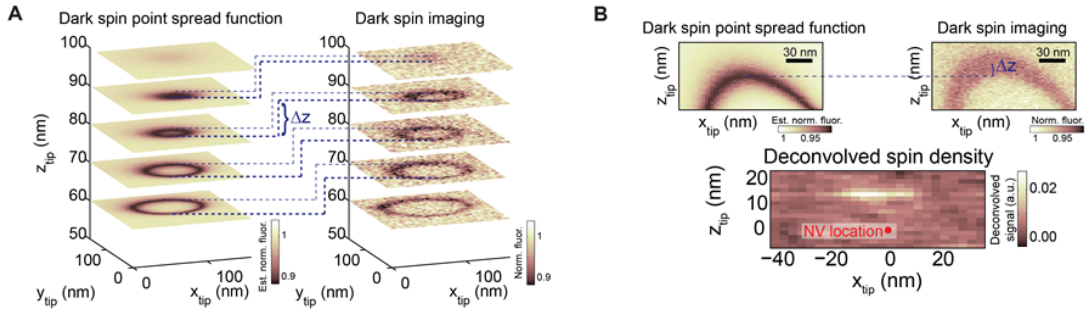

Figure 15: ***(a)*** *Left: dark spin PSF calculated as described in the text. Right: NV-MRI dark spin image. The dark spin image is shifted in the z direction from the PSF.* ***(b)*** *Deconvolution of (a) gives the spatial distribution of the dark spins. As already indicated in (a) the dark spins are vertically shifted by* 14 *nm.*

resonance with the applied RF and will then decohere the NV and decrease its fluorescence.

The PSF can now be compared to the actual measured response of the NV. If the dark spins are shifted from the NV in position, the dark spin response will be shifted from the PSF. If the dark spins are spread out, the dark spin response will be smeared out. Fig. 15 shows the calculated PSF, the dark spin image (a) and its deconvolution (b) giving the spatial distribution of the dark spins. The deconvolution suggests a layer of spins 14 nm above the NV. This value matches the depth of the NV given its implantation energy and indicates that the dark spins are located on the surface of the diamond.

Spins that produce random fluctuating magnetic fields on the NV have been found on the top of the pillar surface but it is still unclear if that they are the reason for the decrease of the spin coherence. Therefore a Monte Carlo simulations has been conducted (see Appendix) in which an NV is sensing nearby spins. The spins are taken to be non-interacting and have a phenomenological T_1-time. The coherence time of the NV is determined from the bath itself. The spin-relaxation time of the dark spins can be measured experimentally and is equivalent to a few mircoseconds. Fig. 16 shows the outcome of a simulation where four spins with T_1 of 3 us are positioned 10 nm above the NV with a spin-spin distance of 1 nm.

The coherence time in this configuration is around 5 us which perfectly agrees with values measured.

Further experiments have shown an interesting correlation between the magnitude of DEER signal and the length of coherence time for different NV-centers. NVs in unprocessed diamond featuring rather long coherence time ($20 - 40$ us) have alomost no DEER signal. In fabricated diamonds it was observed that NVs with

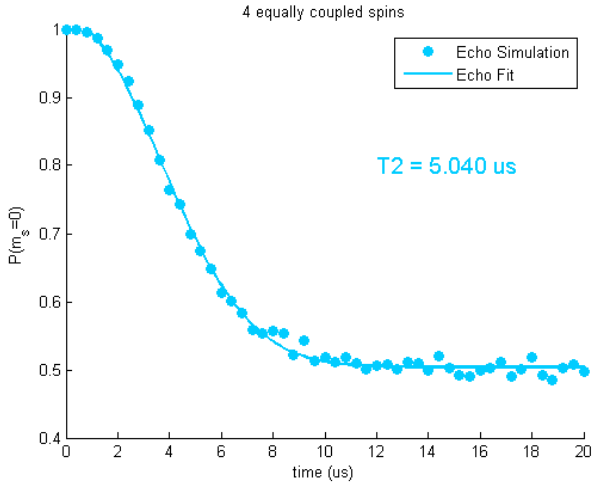

Figure 16: *NV coherence decay as calculated with a Monte Carlo simulation. The decoherence source are four dark spins placed 10 nm above the NV. The T_1 times of the dark spins are 3 us each. The simulation is fitted to $A \cdot e^{(-\frac{\tau}{T_2})^n} + b$ and T_2 is extracted from the fit.*

shorter T_2 are more strongly coupled to dark spins than NVs with longer T_2. These results therefore suggest that the interaction of the NV with paramagnetic dark surface spins is the main reason for the reduced NV coherence in etched diamond nanopillars.

4.2 Discussion

DEER measurements on shallow NV-centers in bulk have demonstrated long coherence times as well as hardly detectable DEER signal. As one etches diamond and forms nanopillars encapsulating a single NV, the coherence time decreases (as shown in Fig. 9) and the DEER signal increases. As far as magnetometry is considered the drop of coherence and additional magnetic noise lead to a decrease of sensitivity.

There is a lot effort made to improve the quality of the NV-center and its environment to further increase the coherence in particular for shallow NVs which are most relevant to sensing. One way is to replace the standard ion implantation process for NV-center creation and thereby avoid crystal damage by a growth method called 'δ-doping' [19]. During the CVD mediated diamond growth a thin ($1-2$ nm) nitrogen-doped layer is created by controlled introduction of Nitrogen gas. K. Ohno et al. have demonstrated long spin coherence times (>100 us) for 5 nm deep NV-centers created by such δ-doping [19]. δ-doping does not only provide long coherence times but also a smaller spread in the depth of the NV-centers compared to ion implantation. However, the NV coherence measured on two different δ-doped diamond samples yields a T2 of 2 and 9 us (see Fig. 17b) as well as a low Rabi oscillation contrast of 5%. Further investigations will be necessary to elucidate the loss of coherence compared to [19].

Shallow NV-centers can also be found in as-grown diamond and exhibit coherence times from 30 to 60 us. In contrast, shallow NV-centers in a polished CVD grown diamond yield a shorter coherence time, due to strain and impurities created during the polishing process (Fig. 17a). Furthermore, the coherence time of NV-centers in nanopillars made from as-grown diamond material is limited to a few us like for ion implanted NV-centers.

Alternatively it has been demonstrated that high temperature annealing improves the coherence time [54, 55]. This approach aims to recover the quality of the NV-center from radiation damage during nitrogen implantation. Normal thermal annealing to form NV-centers takes place around 800 °C typically leading to short coherence times ($\approx$ 40 us) for shallow NVs. This indicates that paramagnetic residuals defects remain in the diamond. Yamamoto et al. demonstrated that high-temperature annealing at 1000 °C gets rid of most impurities allowing for a coherence time up to 2 ms of deep NV centers. Not only the coherence time improves by high-temperature annealing but it also stabilizes the NV-center re-

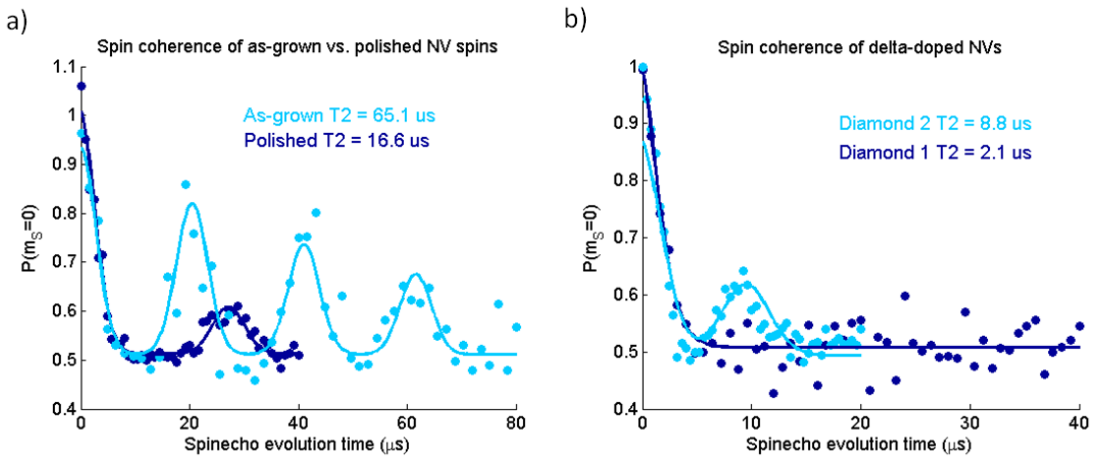

Figure 17: ***(a)*** *Comparison of T_2 between an as-grown and a polished diamond.* ***(b)*** *Spin-echo of two δ-doped diamonds. Both show rather short coherence times and low contrast (not visible).*

sulting in a smaller switching rate from NV^- to NV^0 and close to lifetime limited linewidths of the optical transitions at low temperature [54, 56]. But it might be critical to apply this technique for our purpose because high-temperature annealing burns the first few nanometers of the diamond and, hence, could destroy the shallow $(5 - 15$ nm) NVs.

As the spin bath changes for shallow NV-centers, their coherence time is reduced from 2 ms in bulk to below tens of us. T_2 is further reduced by the fabrication of scanning probes to below 5 us. We have shown experimentally that this reduction is due to the creation of more surface spin during the diamond fabrication. Also Monte Carlo simulations indicate that these surface spins decrease the coherence time to the regime of below 10 us. However, it can not be excluded that there is no other source of decoherence, like fluctuating electric fields from charges trapped at the surface.

5 Pinning of dark spins

As we learned from the last chapter, dark spins on the diamond surface are believed to limit NV coherence times to below 10 us in diamond nanopillars. This chapter presents the idea to pin these dark spins and slow down their flipping rate. This might result in less magnetic fluctuations on the NV and possibly longer coherence time.

5.1 Exchange bias effect

In order to pin the magnetic surface spins, an effect called exchange bias is exploited. The most popular application of the exchange bias effect, the giant magnetoresistance, was awarded the Nobel prize in the year 2007. P. Grunberg [57] and A. Fert [58] observed in 1988 the giant magnetoresistance (GMR) effect in ferromagnetic-nonmagnetic multilayer structure, where the electrical resistance depends on the relative orientation of the magnetization in both ferromagnetic layers. The device resistance yields a minimum (maximum) for parallel (antiparallel) orientation of the magnetization. The GMR effect is the underlying mechanism in a spin valve structure as depicted in Fig. 18a. The spin-valve structure consists of two ferromagnetic layers separated by a nonmagnetic spacing layer. The first layer (reference layer) is pinned via exchange bias by an antiferromagnet (AFM) and the second (sensor layer) is rotatable, i.e. sensitive to magnetic fields. When reading out a magnetic memory the stray field of the single bits can easily rotate the magnetization of the sensor layer but not of the reference layer, resulting in a measurable change of electrical resistance. The GMR effect is thus widely used in reading heads of hard drives. There this gigantic difference in resistance when reading a 0 bit or a 1 bit assures high readout fidelity.

In order to understand the exchange bias effect, it is necessary to explain a hysteresis loop of a basic ferromagnet (FM). The response of the magnetization M on an externally applied field H is epitomized by the hysteresis loop. An example is depicted in Fig. 19. Above the Curie temperature T_C of a ferromagnet, little domains of atomic magnetic moments are completely randomized and the ferromagnet is in an unmagnetized state. Starting from this state at the origin of the loop, in presence of an external magnetic field the magnetization rapidly increases until all domains are aligned with the field at the saturation magnetization $M = M_S$. As the field is reversed the magnetization follows a different curve. At zero field, there is some remaining magnetization called remanence at $M = M_r$.

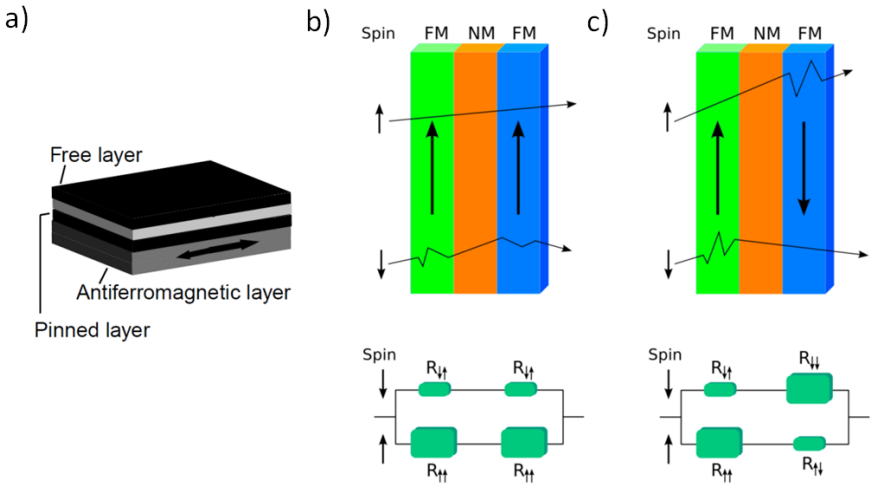

Figure 18: *(a) Spin-valve structure: There is one free ferromagnetic (black) layer on top, a non-magnetic spacing layer (light gray) in between and an exchange biased ferro- (black) and antiferromagnetic (dark gray) layer at the bottom. The top ferromagnetic layer is freely rotatable in an applied magnetic field and is often referred as the sensor layer. The bottom ferromagnetic layer is pinned and should not be rotated by an external magnetic field. This layer is called the reference layer. (b, c) Principle of the GMR effect: The reference layer is green, the sensor layer blue and the spacing layer orange. Below is a cartoon of the resistance for spin up and down polarized current. (b) When the reference and sensor layer are parallel the spin-up polarized current can pass the spin valve easily while the spin-down polarized current gets scattered and experience a large resistance. One observes a low overall resistance. (c) As the reference and sensor layer are anti-parallel both spin-currents experience scatting in one of the layers resulting in an larger overall resistance than in the parallel configuration. Image taken from [59].*

At the coercivity field $H = H_C$ the magnetization of the magnet changes sign. At large negative fields the magnetization eventually saturated again at $M = -M_S$. A ferromagnet is characterized by an easy axis of magnetization. In case of uniaxial anisotropy there are two equivalent easy configurations. The two energetically favorable magnetization points along the easy axis but in opposite direction. The coercivity then has the same magnitude at the points A and B in Fig. 19. The hysteresis loop has point symmetry to the origin.

In 1956 Meiklejohn and Bean reported on 'a new type of magnetic anisotropy' [60]. They investigated hysteresis loops of fine particles of cobalt, another typical ferromagnet. Instead of measuring a symmetric loop, they found it to be shifted along the field axes H as depicted in Fig. 20. A horizontal shift indicates an unidirectional anisotropy, for which there is only one easy configuration along the easy axis for the magnetization. Meiklejohn and Bean found out that these fine cobalt particles are covered by a native oxide which was known to be an antiferromagnet. An antiferromagnet consists of two alternating sub-lattices with opposite spin alignment. This antiferromagnetic order exists only below the Neel

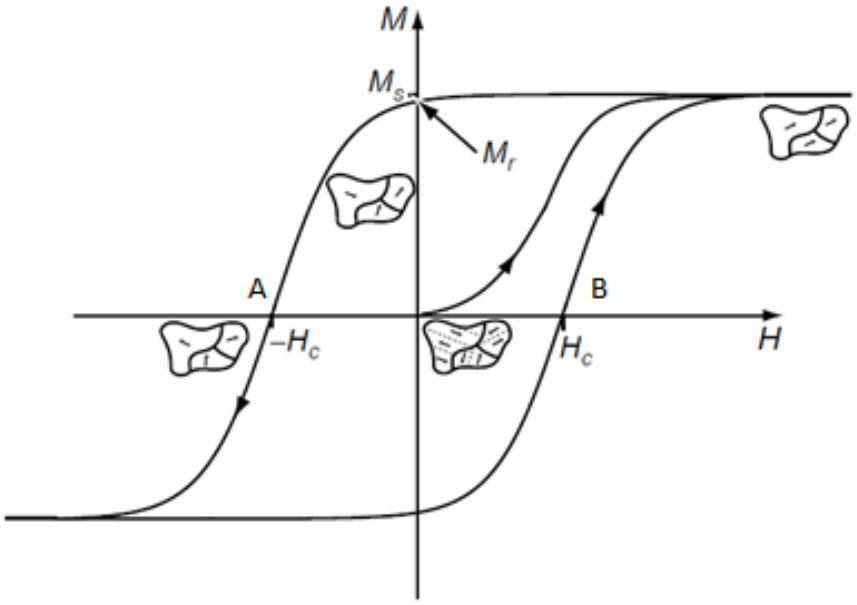

Figure 19: *Hysteresis loop of a typical ferromagnet. When applying an external magnetic field to an unmagnetized ferromagnet, the spin domains start to align themselves with the field until the magnetization reaches saturation. All domains are now aligned with the field. When the field is decreased, the hysteresis loop intersects the magnetization axis at the remanence magnetization at zero field. At the coercive field the magnetization changes sign. Image taken from [59].*

temperature. Meiklejohn and Bean claimed the origin of the exchange bias to be an exchange interaction between the ferromagnet and the antiferromagnet as the hysteresis shift disappeared above T_N. An intuitive sketch of the exchange bias is shown in Fig. 20. For temperatures higher than T_N (Fig. 20 a), the direction of the spins in the AFM are thermally randomized and the AFM has no effect on the FM. The spins of the FM are aligned and the hysteresis curve is symmetric along the applied magnetic field H as in Fig 19. As temperature falls below T_N (Fig. 20 b) the AFM spins start to line up with respect to the FM. The FM spins are still perfectly aligned with the applied field yielding a maximum magnetization. When the applied magnetic field is inverted (Fig. 20 c) the FM spins start to rotate. In case of a high enough anisotropy of the AFM, the antiferromagnetic spins remain unchanged and the exchange interaction at the interface tries to pull back the FM spins. Hence, a higher switching field (compared to no AFM on the FM) is required to flip the ferromagnetic spins and to invert the magnetization (Fig. 20 d). As the field is reversed again a microscopic torque favors the rotation of the ferromagnetic spins and only a small field is required to flip the spins. As a consequence the whole hysteresis loop is shifted horizontally along the field axis yielding a unidirectional

anisotropy. There is only one easy configuration meaning the spins are pinned [61].

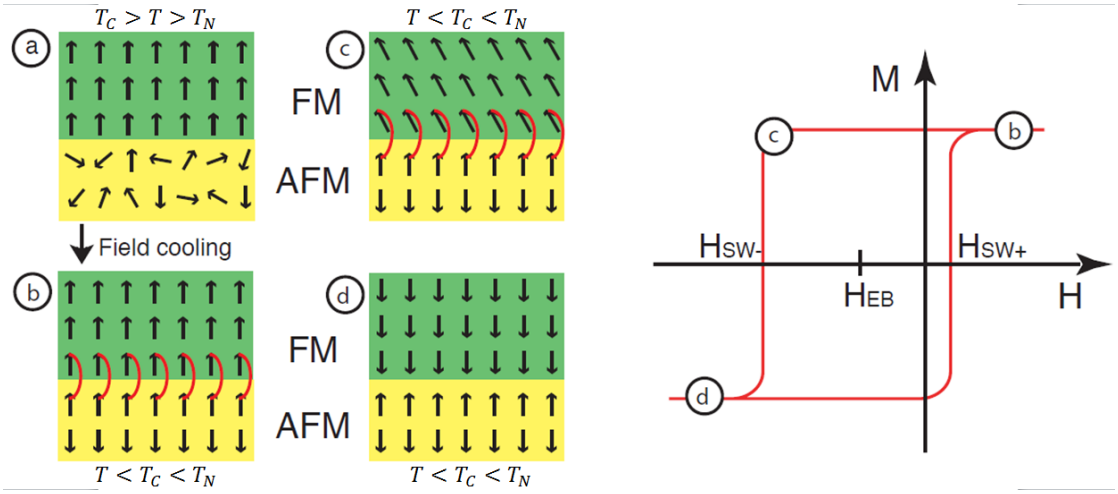

Figure 20: ***(a)*** *The temperature is above the T_N but below T_C, such that the spins of the AFM (yellow) are disordered but the spins of the FM (green) are ordered.* ***(b)*** *After cooling below T_N the AFM forms two sublattice with opposite spin alignment.* ***(c)*** *An external magnetic field is aligned in opposite direction to the FM spins and slowly increased. The spins start to rotate with the magnetic field, but the exchange interaction of the AFM with the FM apply a torque on the AFM spins.* ***(d)*** *The magnetic field necessary to invert the magnetization is therefore shifted to larger negative values. Image taken from [62].*

5.2 An antiferromagnet on top of diamond

In order to pin dark spins on the surface of diamond nanopillars, an antiferromagnet with certain specifications is required. First of all, the Neel temperature has to be higher than room temperature. Second, the AFM should be an insulator to avoid quenching of the NV fluorescence as well as thermally induced current in the AFM which would produce random magnetic fields at the NV-center. A suitable candidate for this purpose would be nickel oxide (NiO) with $T_N = 524$ K since it has been shown that NiO exhibits exchange bias in structures having a width comparable to the pillar size [63].

Pillars with a diameter of 195 nm have been fabricated on a (100) orientated diamond with shallow NV-centers ($3 \cdot 10^{11}/\text{cm}^2, 6$ keV) and many pillars obtaining single NV-centers have been characterized with T_2-times between 1 us and 6 us. Then nickel oxide was formed on the diamond surface by thermal evaporation (Sharon Thermal Evaporator, Sharon) of 20 nm nickel onto the diamond and subsequent oxidation process (30 min, 580 °C, 5000 SCCM O_2 flow, RTP-600xp, Modular Process Technology) [64, 65]. Due to lack of knowledge this process was not suitable for diamond since diamond gets etched by oxidation at temperatures

above 500 °C [66]. The etch process is even catalyzed by metal particles like nickel [67]. Interestingly this process etches diamond anisotropically with the [111] crystallographic orientated planes the slowest as can be seen in Fig. 21. This is also reported in [68]. After this process all NV-centers were etched away.

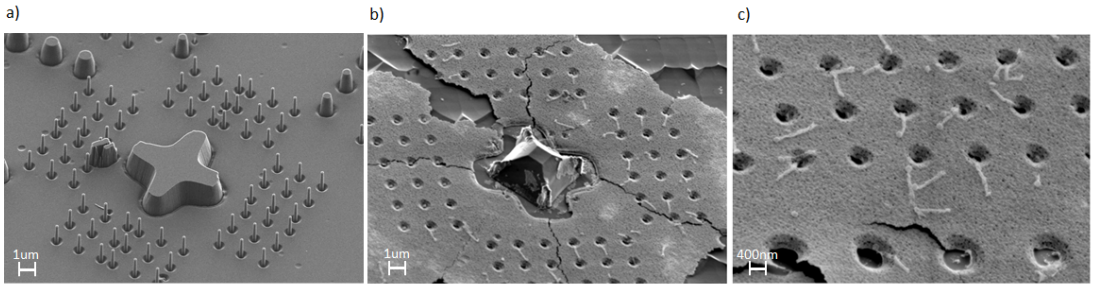

Figure 21: ***(a)*** *Pillars and markers after etching.* ***(b)***, ***(c)****: Pillars and markers after nickel evaporation and subsequent annealing in an oxygen-atmosphere. On the basis of the marker, it can be easily seen that the etching is anisotropic in nature.*

Since forming NiO by oxidation of evaporated nickel destroyed all shallow NV-centers, nickel oxide was sputtered from a pure nickel target in oxygen atmosphere. Conditions for reactive sputtering of NiO can be found in literature [69, 70] but will only match the sputtering machine used in the paper. Hence, tests with various sputtering conditions have been done. Reactively sputtered nickel oxide (150 W with 40 SCCM argon and 16 SCCM oxygen, ATC, AJA International) was confirmed by ellipsometry (N = 2.157 , literaure:
N = 2.1818, LSE-W, Gaertner Scientific) and XPS (Thermo Scientific K-Alpha XPS, Thermo Scientific) as depicted in Fig. 22.

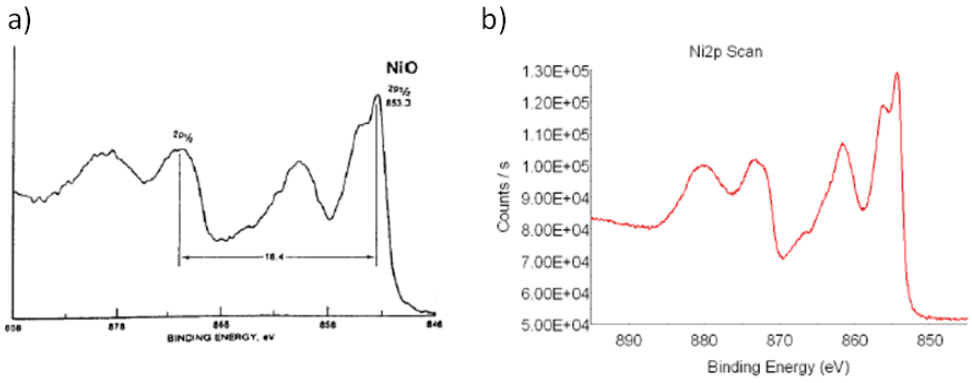

Figure 22: *Comparison between XPS binding energy found in literature* ***(a)****[71] and measurement of reactively sputtered NiO* ***(b)****.*

30 nm NiO was sputtered onto an unprocessed diamond ($3 \cdot 10^9/\mathrm{cm}^2, 6$ keV) and spin-echo multiple NV-centers were measured before and after deposition.

5.3 Results

The outcome of the measurements is displayed in Fig. 23. The average T_2 of the untreated NVs is around 10 us and 12 us for the NiO covered NV-centers. In both cases most NV-centers had rather short coherence times between 1 and 10 us and a few NVs had coherence time as long as 56 us. The large variance in T_2 most probably reflects the variance in NV-depth. However, when comparing the non covered NV-centers with the NiO covered NV-centers no significant improve can be observed.

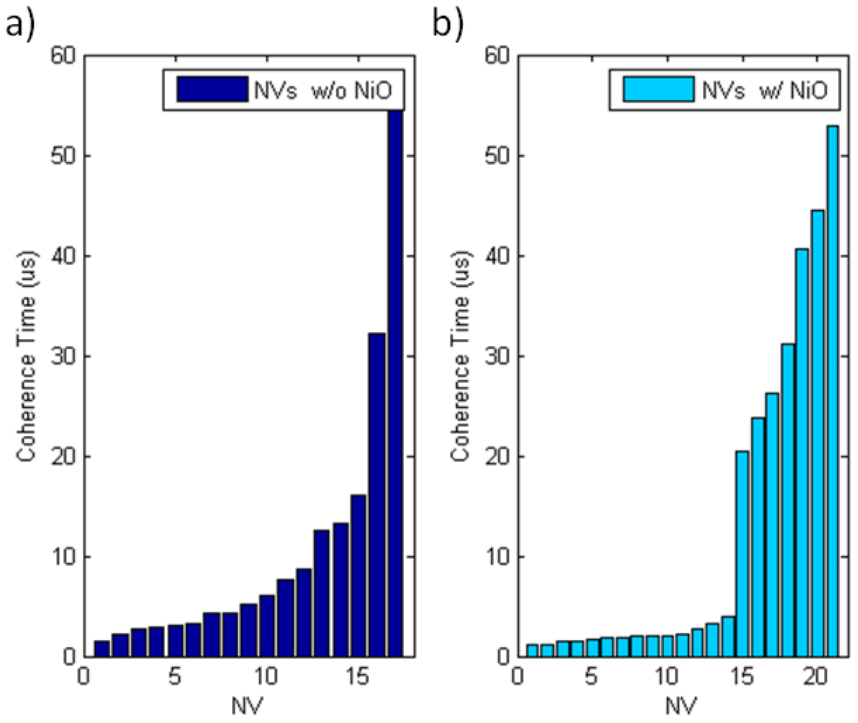

Figure 23: ***(a)*** *T_2 of NVs before deposition of nickel oxide. The average T_2 of the reference is 10 us.* ***(b)*** *The coherence times of NVs covered with 30 nm NiO are plotted. The average T_2 is roughly the same.*

Out of these measurements four NV-centers were measured before deposition and re-identified after deposition. The spin-echo of those four NVs is fit to $C * exp(-\frac{\tau^n}{T_2^n}) + b$. Fig. 24 displays the parameter T_2 and n of the fit before and after NiO deposition.

As can be seen, the coherence time stays on average the same. The exponent of the fit changes much more, but no clear tendency is seen for the case with or without nickel oxide.

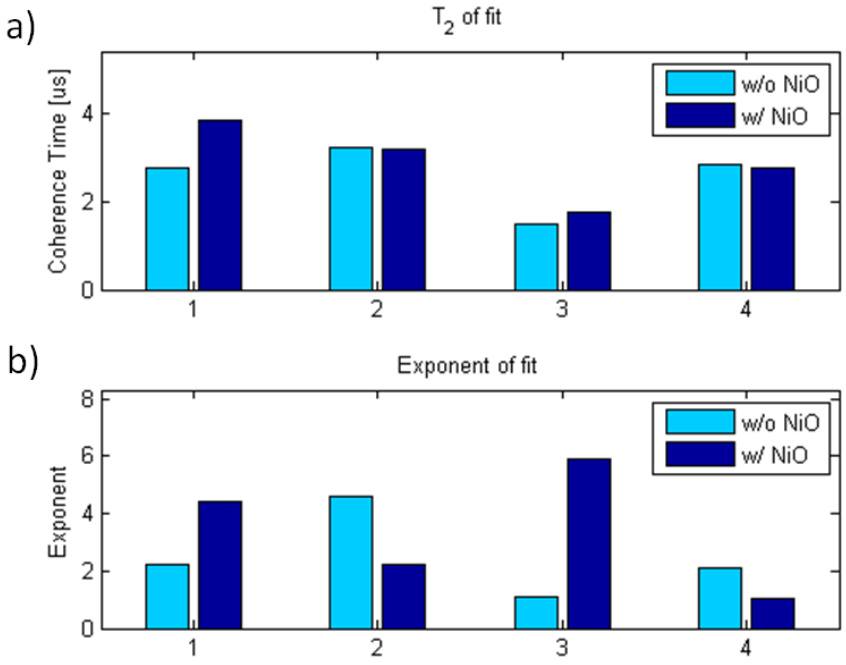

Figure 24: ***(a)*** *T_2 of four NVs before (bright blue) and after (dark blue) deposition of nickel oxide.* ***(b)*** *Power index of the fit for the same four NV-centers.*

5.4 Discussion

Overall pinning does not appear to be simple and we have not observed any direct effect of pinning on the coherence time of NV-centers. There are a lot of parameters involved like roughness, grain size or the quality (crystallinity) of the nickel oxide. It is known that it is possible to pin many layers of ferromagnetic spins but not how that converts to single paramagnetic impurities with a spin-spin distance of about one nanometer. Further, if there is exchange biasing of the dark spins at all, it is questionable if the pinning of the spins is sufficient to observe a change in coherence time. In order to exclude all of these questions it might be smart to work together with a group that focuses its research on exchange biasing.

In addition, even if the dark spins on the diamond surface could be pinned that does not necessarily go along with an increase in coherence time. When imagine a single paramagnetic impurity interacting with a single NV-center there are two extreme cases as for the coherence time. In the first scenario the spin-relaxation time of the dark spin is infinite and it never flips during a spin-echo. The spins produce a static magnetic field whose phase gets refocused after the π-pulse in a Hahn-echo sequence and it has no effect on the NV-center at all meaning it does not cause decoherence. The envelope of the spin-echo is a Gaussian function. The second scenario is a spin with super short T_1. The spin would flip at an extremely fast rate. Like for the non-flipping spin, this would not effect the NV at all since it

motionally narrows out. The envelope of the spin-echo is an exponentially decaying function. In between those two cases there is a coupling rate corresponding to the free evolution time of the spin-echo for which the NV-center picks up maximum phase and gets maximally decohered. This behavior can be reflected using the same Monte Carlo simulation described in section 3. But this time many spin-echos are simulated with four dark spins located on the top of a pillar featuring various T_1-times. Coherence time of the NV versus T_1 of the surface spins is sketched in Fig. 25.

Now why is a pinning of dark spins not necessarily an improve in coherence time? Assuming the surface spins are in the exponentially decaying regime (fast flipping spins, right side of the curve), pinning them could slow them down into regime that affects the coherence time of the NV even more (center of curve). In that case pinning of surface spin is disadvantageous. This is why Fig. 24 also shows the exponent of the fit to estimate in which regime the surface spins are in before and after deposition of NiO. However, based on the data shown, it is difficult to make a clear statement.

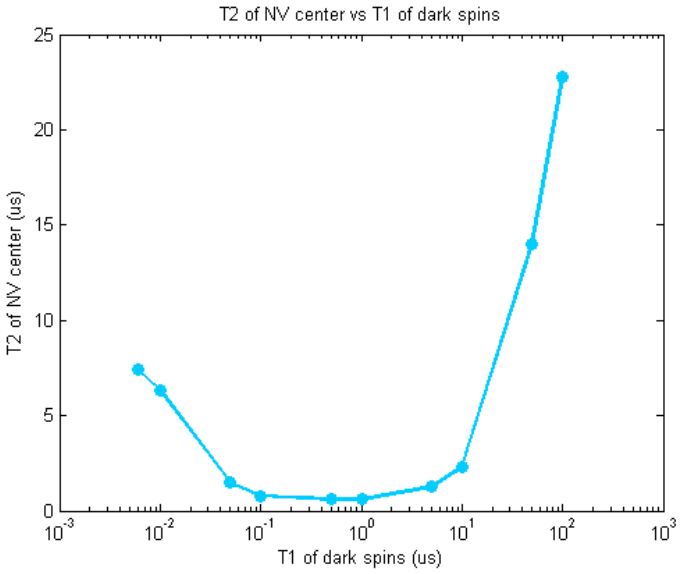

Figure 25: *The coherence times of an NV near four dark spins is calculated for various spin-relaxation times of the dark spins. The coherence time gets huge for extremely slow or fast flipping dark spins. For T_1 of 500 us the coherence time of NV is 123.2 us. However, as T_1 of the dark spins increases further, other decoherence sources might get dominant.*

As a last point, it is arguable if the exchange bias is the right way to go anyway. Even if it works would we gain at all? Therefore we have to remind us of the dependence of the magnetic field sensitivity. In the best case the sensitivity is proportional to $\sqrt{T_2}$ but the magnetic field decays as $1/r^3$. Assuming the thickness of AFM layer sufficient to pin the spins is only 5 nm, increasing the sensor to sample distance from 10 nm to 15 nm, the coherence time needs to improve by a factor of ≈ 11 to only maintain the same sensitivity.

To summarize we were not able to successfully pin the dark spins, i.e. increasing significantly the coherence time by deposition of an antiferromagnet. Exchange biasing is a complicated subject and its actual use is arguable. Therefore I tried a different approach. There, the idea was not to recover the coherence but avoid its decay a priori by changing the fabrication process.

6 Alternative fabrication of diamond nano-pillars

As discussed during the etching of pillars, dark spins are created at the surface of diamond and a drop of coherence is observed. This chapter will give an overview of the current etch process and I will point out which steps within this particular process might cause the creation of the spins and how to possibly get around it. An alternative pillar fabrication process and measurements of coherence times in these devices are presented.

6.1 Current fabrication process

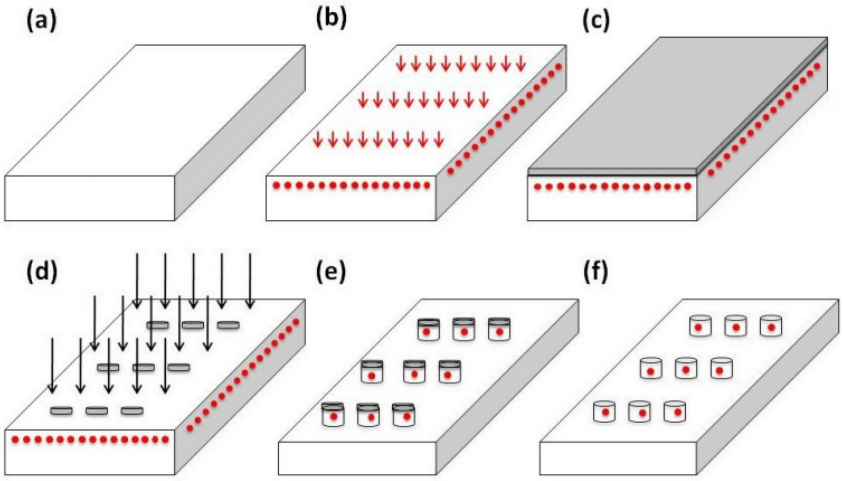

Figure 26: ***(a)*** *The process starts with a thin slab of diamond.* ***(b)*** ^{14}N *is implantated at a density of* $3 \cdot 10^{11}/cm^2$ *with 6 keV energy and subsequently annealed to form shallow Nitrogen-Vacancies (red points) [72].* ***(c)*** *The diamond is masked with a negative electron lithography resist (gray layer).* ***(d)*** *The resist is exposed and developed to obtain a cylindrical etch mask 200 nm in diameter.* ***(e)*** *Pillars* $(1 - 2$ *um in length) are etched into the diamond using reactive ion etching.* ***(f)*** *The remaining etch mask is removed with an HF wet etch. Figure taken from [41].*

Pillars are fabricated by patterning a resist with electron-beam (e-beam) lithography and subsequent oxygen etch as illustrated in Fig. 26. Nitrogen atoms are implanted at an energy of 6 keV at a density of $3 \cdot 10^{11}$ cm^{-2} into an electronic grade diamond from Element Six. Subsequent annealing at 800 °C for 2 hours forms shallow NV-centers approximately 15 nm below the diamond surface. To remove graphitic carbon and any other surface contamination the diamond is cleaned for one hour in a 1:1:1 refluxing mixture of boiling sulfuric, perchloric and nitric acids. Next two e-beam resists - XR and FOX 16 (flowable oxide, Dow Corning) - are spun onto the diamond (3000 rpm, 40 s) and baked at 120 °C for

5 minutes, at 180 °C for 10 minutes and at 120 °C for 15 minutes yielding an about 600 nm thick resist layer. A pillar pattern is written into the resist using e-beam lithography (100 keV, 60000 dots, 100 pA, 11200 uC/cm^2, ELS-F125, Elionix). The resist is developed in 25% Tetramethylammonium hydroxide (TMAH) for 17 s leaving cylindrical silicon oxide etch masks on the diamond surface. The mask is transferred into the diamond with an oxygen plasma etch (5 min, 700 W ICP, 100 W Bias, 30 SCCM oxygen, Unaxis, Shutterline ICP). As a last step, the remaining mask is removed with an Hydrogen fluoride (HF) wet etch.

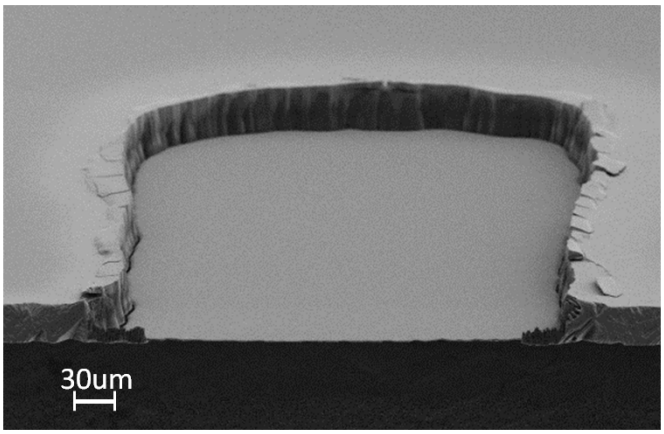

Figure 27: *A thin slab of diamond. A small section within a 50 um thick diamond is etched down to a few um thin slab. FOX pillars have better adhesion to region of the slab near the edge compared to the center. This is most probably due to vibrations of the thin slab.*

As the source of decoherence is created during the fabrication process and is located on the top surface of the pillars it is obvious that something goes wrong on the diamond-etch mask interface during the fabrication process. And indeed there are a few indications that the etch mask FOX is not ideal, i.e. FOX might be the issue during the process and replacing it by a more sophisticated etch mask might solve the problem. First of all the adhesion of FOX to diamond is rather poor such that an additional thin layer of XR (Dow Corning) is first spun onto the diamond acting as an adhesion layer. Still after writing pillars on a thin slab (as depicted in Fig. 27) and development in TMAH, almost 50% of the pillars are washed away. This poor adhesion might as well be the main problem during the etch process. It is reasonable to assume that oxygen plasma, that etches the diamond, can sneak under the etch mask and modifies the top surface layer of the diamond in some unknown way. This assumption is supported by the fact that pillars with a diameter of 500 nm and, hence, a better aspect ratio and presumably better

adhesion, do not show the decay of decoherence. Furthermore when investigating coherence time versus DEER signal on a thin slab it is clearly visible that the coherence time towards the edge of the thin slab increases along with a decrease in DEER signal while the coherence time in the center of the slab is minimized with a maximized DEER signal. This can be explained in terms of vibration of the thin slab. Compared to the center of the thin slab, the thickness of the slab increases towards the edge of the thin slab and vibrations are damped more, FOX pillars stick better and less oxygen can sneak under the mask. This gives a reasonable connection between adhesion of the mask, dark spin abundance and coherence time. Next when FOX pillars are imaged with a scanning electron microscope (SEM, 3 keV) it can be seen that the FOX melts at little bit. This looks like FOX is not too temperature stable and there might be some chemical reactions going on inside the etching chamber where high temperatures are reached during the etch process. However, there is no further evidence that chemical reactions are actually happening leaving this assumption rather speculative. Still, we tried to investigate the chemical composition of the first few nanometers of the pillars using X-ray photoelectron spectroscopy (XPS). But assuming already a whole monolayer of chemical dirt on the surface, due to proximity effects it is not possible to reach a high enough pillar density to exceed a critical quantity to be detected with XPS. However, there are enough indications that justify to try a different etch mask with a better adhesion. After discussing this issue with various people fabricating diamond it emerged that alumina (Al_2O_3) is a good choice.

6.2 Alumina as an etch mask

N. de Leon et al. use alumina as an etch mask to fabricate free standing triangular beams in diamond as reported in [73]. The advantage of alumina compared to FOX is its high etch resistivity. The etch resistivity of alumina corresponds to 200:1 (Al_2O_3 : diamond in oxygen plasma) while FOX has a resistivity of 6:1 (FOX : diamond). This implies that for etching the same length of pillars a much thinner alumina mask is sufficient leading to a much better aspect ratio and adhesion.

6.2.1 Lift-off process

The process involves patterning of PMMA, deposition of alumina and lift-off. It is illustrated in Fig. 28.

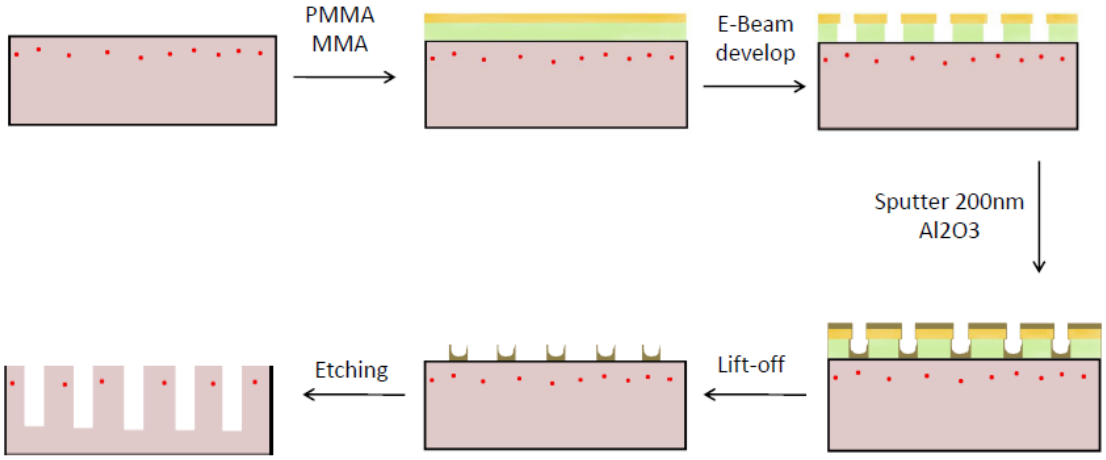

Figure 28: *MMA (green) and PMMA (yellow) are spun onto a diamond containing NV-centers (red points). The resist is patterned using e-beam lithography and developed. About 200 nm alumina (golden) is sputtered into the holes using reactive sputtering from a pure aluminum target. The resist is lift-off in acetone leaving cylindrical pillar masks. The diamond is etched with an oxygen plasma in a reactive-ion etcher.*

Pillars are fabricated from a high-purity diamond sample with nitrogen implanted ($3 \cdot 10^{11}$ cm^{-2}, 6 keV) and subsequent annealing at 800 °C. After acid cleaning the diamond, a copolymer resist (MMA EL9, Microchem) and PMMA (950 C2, Mircochem) is spun onto the diamond at 5000 rpm yielding a 250 nm thick MMA and 150 nm thick PMMA layer. The diamond is hard baked for 5 min at 180 °C. Before e-beam lithography a conducting layer of Espacer (Showa Denko) is spun. The pattern is written with e-beam lithography (100 keV, 20000 dots, 1 nA, 2133 uC/cm^2). The diamond is rinsed with DI and developed for 60 s in 1:3 MIBK:IPA. Then 200 nm alumina are reactively sputtered into the holes (400 W, 15Ar/3O_2, 4 mTorr, Orion 3, AJA). The resist is lift-off in acetone. The MMA holes are typically a little broader than the PMMA holes providing a breaking point as indicated in Fig. 28. The pillars are now etched as described previously. As it turns out, the lift-off method is not applicable for etching pillars of 1.5 um length because the mask is too thin as shown in Fig. 29 a). The aspect ratio of the holes (200 nm in diameter and 400 in height) makes sputtering into it rather difficult. As one keeps etching pillars after they are about 1 um long, the pillars start to taper and the NV-centers get destroyed. When choosing a thinner MMA layer to alleviate filling of the holes, the lift-off becomes almost impossible.

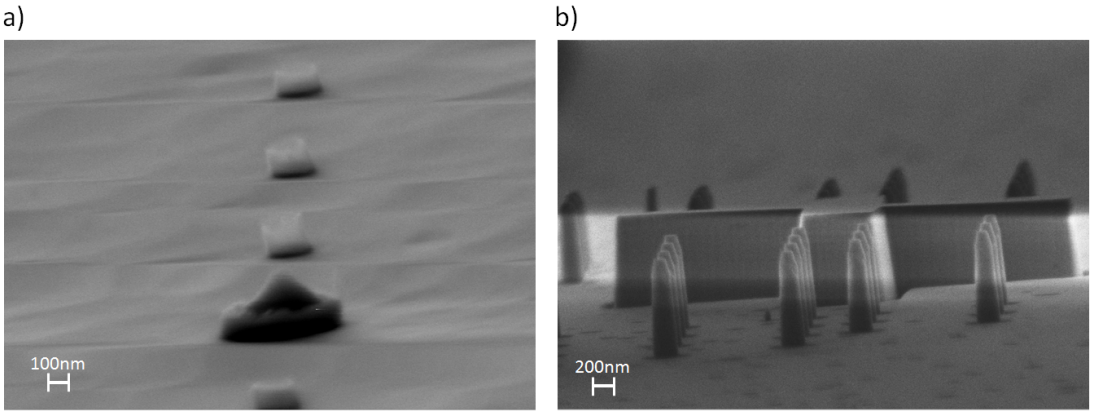

Figure 29: ***(a)*** *Alumina mask after lift-off. The size of the two different masks are 200 nm for the small ones and 500 nm for the big ones. It can be seen that the small ones are cup-like shaped with only a very thin ground.* ***(b)*** *1.3 um tall diamond pillars that already look tapered at the end.*

Since the lift-off process did not work, I tried a different method which I call the 'ZEP-method' because of the usage of the e-beam resist ZEP 520 (Zeonrex Electronic Chemicals).

6.2.2 ZEP method

ZEP is a high performance positive e-beam resist that shows high resolution and high dry-etch resistivity. The fabrication process is sketched in Fig. 30. The final etch mask is again alumina and it is patterned by mask transfer.
After acid cleaning, 70 nm high quality alumina is deposited on the diamond using atomic layer deposition[5] (ALD, S200, Cambridge NanoTech). The diamond is solvent cleaned in cold acetone and IPA for 5 minutes before removing organic contamination from the surface using gentle oxide plasma (220 Technics, 300 mT, 100 W, 10 SCCM O_2, 5 min). The diamond is then pre-baked at 180 °C for 5 min. Since ZEP loses adhesion to the alumina when a layer of water is in between, the water is removed by spinning Hexamethyldisilazane (HMDS) and baking at 180 °C for another 2 min. Then the diamond is transferred quickly onto a spinner and pure ZEP is spun. Spinning at 4000 rpm yields a ZEP layer thickness of 300 nm. Finally Espacer is spun and a negative pattern is written using e-beam lithography (100 keV, 20000 dots, 1 nA, 257 uC/cm^2). Espacer is removed in DI water and ZEP

[5] I also tried reactive sputtering of alumina but it seems that the oxygen plasma inside the sputtering machine already attacks the top surface of the diamond and either decreases the surface quality or even etches away the NV-centers.

is developed in O-xylene for 90 s. The mask is transferred into alumina using RIE (7 cycles a 15 s 400W ICP, 150 W Bias, 8 SCCM BCl_3, 2 SCCM Cl_2.). Afterwards diamond pillars are etched using slightly different etch parameters than for FOX pillars. The alumina mask shows indication of erosion resulting in slightly tapered diamond pillars. In order to counteract that the ICP power is increased to 900 W and the Bias power decreased to 80 W to etch more chemically (isotropic).

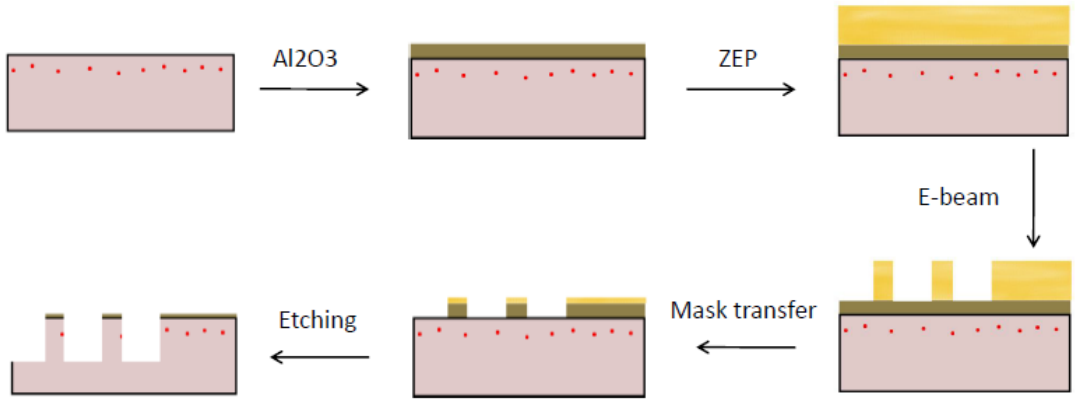

Figure 30: *About 70 nm alumina (golden) is deposited onto diamond using ALD. After various cleaning steps and preconditioning, ZEP (yellow) is spun and hard baked. The pattern is written via e-beam lithography and developed in O-xylene. A mixture of boron trichloride and clorine plasma transfers the mask into alumina. Diamond pillars are then etched using oxygen plasma.*

Another advantage of ZEP is the masking of diamond that does not get structured. Since ZEP is a positive resist, ZEP is only removed during development where hit by the electron beam. This means ZEP is only removed inside the writing fields, whereas FOX is removed everywhere except for the pillar mask. Ergo the alumina still covers the whole diamond except for the written fields and protects so the NV-centers underneath during pillar etch. When using FOX it is necessary to protect the unpatterened diamond with an additional quartz plate that is manually placed onto it.

Fig. 31 shows the difference between the FOX and the alumina mask. As already mentioned as alumina has a much higher etch-resistivity less mask is required for etching the same pillar length as for FOX. This results in a better aspect ratio and better adhesion. The alumina mask can even stand sonication in acetone proving good adhesion. According to our theory, better adhesion should result in better protection of the pillar top surface during the etch process and higher NV quality with longer coherence compared to FOX.

A scanning electron microscope image of the diamond pillars produced by the

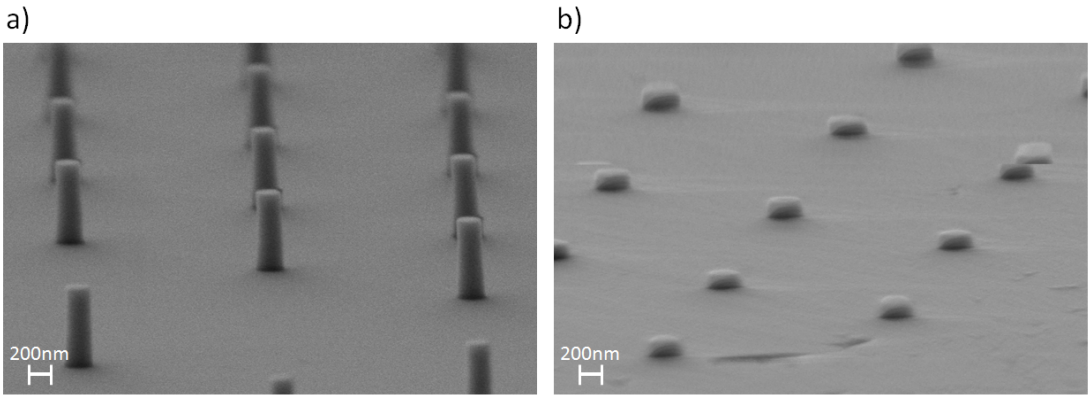

Figure 31: ***(a)*** *Fox pillars are 600 nm tall and 200 nm in diameter giving an aspect ratio of 3.* ***(b)*** *Alumina pillars are 70 nm tall and 200 nm in diameter giving an aspect ratio of 0.35.*

ZEP-method is shown in Fig. 32. Although the pillars are still slightly tapered the count rate are comparable to pillars with straight side walls.

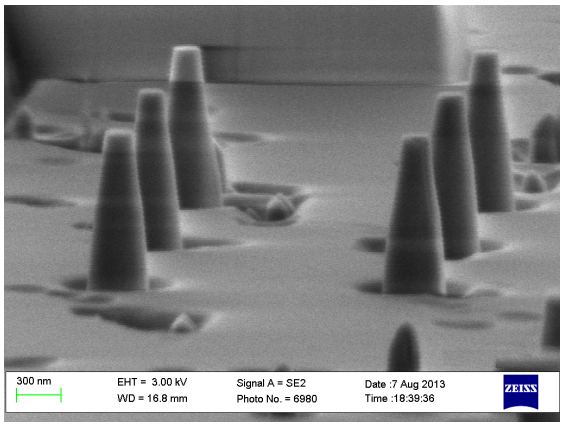

Figure 32: *Diamond pillars fabricated using the ZEP-method. The pillars are 200 nm in diameter at the top and around one micrometer long.*

6.3 Results

11 random positions on an unpatterened diamond (nitrogen implanted with 6 keV,$3 \cdot 10^{11}/\text{cm}^2$) were investigated. Each position contains many NVs within the confocal spot. Hence, an averaged bulk coherence time is measured for each position. Then the diamond is patterned as described before. Again 11 pillars with single NV-centers inside were investigated and a spin-echo measured. Searching for single NVs was a bit biased in that bright pillars were preferentially investigated. But this is justifiable since the same biasing is applied when investigating pillars made with FOX as a mask. The result of the measurements is shown in Fig. 33.

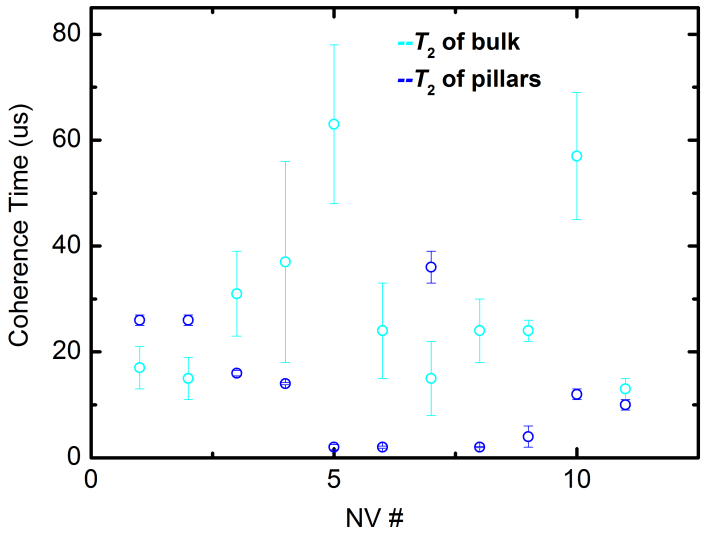

Figure 33: *The plots show coherence time versus random NV-centers in bulk (bright blue) and in nanopillars (dark blue).*

The coherence time of shallow bulk NV-centers ranges from 15 us to 63 us. The minimum coherence time for an NV in a pillar measured is 2 us and the maximum coherence time 36 us. On average the coherence time of the NVs in pillars is lower than in bulk, but there is no dramatic decay. As far as FOX pillars are concerned almost every pillar investigated by us has coherence time around $2 - 4$ us. Here only three NV-centers have T_2 far below 10us. Six NVs have T_2 from 10us to 20 us and even two have coherence time as long as 32 us.

6.4 Discussion

It is known that FOX pillars have a very poor adhesion to diamond, especially to thin slabs where the yield is less than 50%. There are additional indications (correlation between coherence time versus position on a thin slab) that could point out that the short coherence time of FOX pillars are linked to this poor adhesion feature of the mask. Hence, it is worth a try to replace FOX with a material that has a better adhesion a priori. Further the smaller aspect ratio due to higher etch-resistivity makes the adhesion of the alumina mask even better.
Although the lift-off process did not work out there is a second fabrication method to get nice alumina etch masks. NV-centers in diamond nanopillars etched with an alumina mask show clear tendency towards longer coherence time. The NV-centers investigated have 2-4 times longer T_2 than NV-centers in FOX pillars. Because of better adhesion not only the coherence time should be better but also the yield on a thin slab which has not been tested so far.
It would be nice to see if this method is reproducible both on a different diamond with shallow NV-centers as well as on a thin slab. Currently the etched pillars are slightly tapered due to erosion of the mask. In order to get vertical side walls some more work needs to be done to fine tune this process.

7 Spin Labels and Spin Amplification

Before the ZEP-method worked out and provided us with promising coherence time in pillars we tried to sense spin labels that are external to the diamond. A spin label is an organic molecule which possesses an unpaired electron, usually on a nitrogen atom, and has the ability to bind to another molecule. The ultimate goal is to attach spin labels to specific amino acids in proteins of a living cell and to sense the unpaired electron of the spin label with nanometer resolution and refer from these measurements information about the structure of the protein, its local environment or dynamics. In a first shot spin labels dissolved in methanol were dropped onto a diamond sample with pillars. This process is also called dropcasting. 4 NVs were measured before and after dropcasting the spin labels. 2 out 4 showed a clear decrease of coherence as depicted in Fig. 34. The spin labels were not driven. Decoherence stems from T_1 decay of the spin labels only.

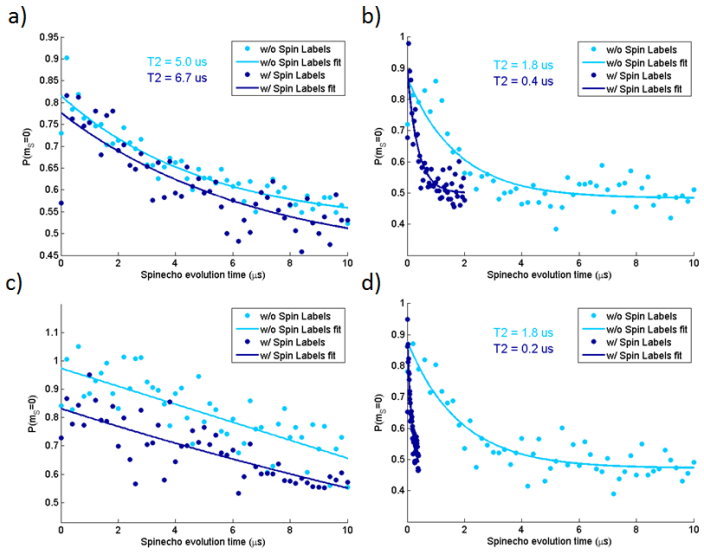

Figure 34: *Before (bright blue) and after (dark blue) dropcasting spin labels onto NVs in diamond pillars. The coherence time of two NV-centers remain unchanged* ***(a,c)*** *after dropcasting spin labels while the coherence time of two other NV-centers has noticeably changed* ***(b,d)****.*

So far B. Grotz et al. have shown sensing of small ensembles of electrons spin on the surface of diamond using double electron-electron resonance [51]. In 2011 H. Mamin et al. detected signal from only 25 electronic spins outside the diamond using the same technique [52]. Two years later they detected proton NMR originating from millions of protons in PMMA that was dropcasted onto diamond [74]. Another year later T. Staudacher et al. pushed the limit even further and applied NMR spectroscopy to sense 10^4 nuclear spins in PMMA [75].
On the way to sense spin labels in biological system our first goal is to sense as few electron spins as possible. The idea was to to tune the spin density by dissolving the spin labels (Tempo, Sigmar Aldrich) in PMMA and spinning onto the diamond.

Therefore a unprocessed diamond with shallow NVs was required.
First we tried to reproduce the decrease of coherence time by simply dropcast spin labels on that diamond ($3 \cdot 10^9$ cm^{-2}, 6 keV, single NVs resolvable). In contrast to the measurement in Fig. 34 on pillars, this time we could not detect any decrease of coherence. In fact we could not identify a single NV-center because the count rate of NVs in bulk was too low to be distinguished from background fluorescence of the acetone/spin label mixture. Therefore we continued with dissolving spin labels in PMMA and spinning onto diamond. 20 NV-centers were characterized before and the very same again after spinning.
We investigated films with spin-spin distance ranging from 0.5 nm to 4 nm and varied the baking temperature from 80 °C to RT. However, there was no evidence of decoherence. To check the status of the spin labels we studied them dissolved in acetone and PMMA using electron paramagnetic resonance (EPR). A reasonably large EPR signal from the spin labels could be observed.
Since there was no detectable decrease in decoherence from the spin labels we decided to actively drive them using DEER. As DEER measurements take rather long for NVs in bulk with low count rates we decided to change the setup to an oil-immersion setup which has not been ready at the time I finished this work.
Meanwhile we changed topics quite a bit and determined if the dark spins on top of our pillars are any useful. In 2011 M. Schaffry et al. proposed a model in which an electronic spin sitting at the end of a diamond nanocrystal acts as an amplifier that directly senses the local magnetic field [12]. It is almost impossible to detect single nuclear spins with shallow NVs, because the two are too weakly coupled. As described previously the magnetic moment sensitivity of an NV-center can be increased by bringing the NV closer to the sample at the expense of decreasing coherence time. The idea now is not to bring the NV-center closer but attaching an additional electronic spin on the end of the diamond. The amplifier spin can be brought extremely close to the sample to be measured. Thereby the amplifier spin can be strongly coupled to a nearby nuclear spin and the NV is still strongly dipole coupled to the amplifier spin because it is an electron spin with a large magnetic moment. Calculations estimate an improvement in magnetic moment sensitivity to be of about 3 orders of magnitude (see Fig.35).
However, the amplifier spins need to fulfill a few requirements for this to work. First one has to coherently manipulate the spins. Therefore T_2^* of the amplifier spin needs to be longer than the Rabi period. Second the coherence time of the spins needs to be at least 1 us long in order to detect a nuclear spin being 1 nm apart.

Last but not least the amplifier spin state needs to be read out with the NV-center. Therefore T_1 of the spin needs to be sufficiently long. If the spin flips before the information is transferred to the NV, the information is lost. Sophisticated pulse sequences unveil that the coherence time of the dark spins on the diamond pillars are only about 250 ns long ($T_2^* \approx 40$ ns) and unfortunately too short to detect nuclear spins.

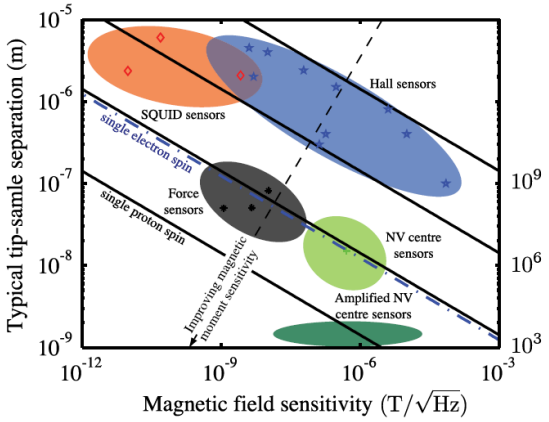

Figure 35: *The plot displays magnetic field sensitivity on the horizontal axis versus typical sensor-sample separation. The line sketches for single electron and proton sensitivity assumes a one second integration time. Figure taken from [12].*

7.1 Discussion

Although we have seen clear evidence of the interaction of dropcasted spin labels with NV-centers in pillars, we could not reproduce this result on a bulk diamond. The spin labels seem to have T_1 being long enough (412 ns), to be measured. However, it is unclear if the interaction with the laser or the host material (PMMA) changes the properties of the spin label. Due to the low count rate of NVs in bulk and the high background fluorescence of dense spin labels it was not possible to put the same high density of spin labels on bulk as on pillars. Assuming the spin labels do not degrade in any way (which is feasible because we already detected them in a comparable environment) the next step is to actively drive them which is to be done.

The detection of single nuclear spins is an enormously challenging and desirable goal and not yet feasible with a single NV-center. However, according to [12] detecting single nuclear spins becomes realistic using an amplifying spin extremely close to the sample of interest. As we get electronic spins at the end of the diamond pillar as an (unpleasant) side effect and no sophisticated attachment of spins is necessary it is definitely worth trying to harness that. Unfortunately a small

ensembles of dark spins at the end of the pillars do not fulfill the requirements. But the properties of a single dark spin has not been investigated yet and it could as well be that a single dark spins, that is not interacting with others, has the potential to serve as an amplifying spin.

8 Summary

NV-centers embedded in monolithic diamond scanning probes have proven outstanding performance in the detection of tiny magnetic fields with subnanometer resolution and high magnetic field sensitivity. So far a single electronic spin under ambient conditions was imaged using this approach [76].
Unfortunately the current fabrication of the scanning probes limits an increase in sensitivity and pushing this technology further to the detection of protons. As we have seen the magnetic field sensitivity is inversely proportional to the optical contrast, the number of photons collected per unit time and the coherence time of the NV-center. The optical contrast is inherent to the NV and fixed, methods to efficiently collect the photo-fluorescence of NV-centers have been presented shortly and the coherence of the NV-center in diamond scanning probes was investigated in detail in this thesis.
It has been observed that the coherence of NV-centers in pillars is dramatically worse in contrast to NV-centers in bulk. A magnetic resonance imaging technique using a scanning magnetic tip and double electron-electron resonance then unveiled the existence of ubiquitous dark spins on the top surface of our diamond nanopillars while NV-centers in bulk show hardly no DEER signal. Further the outcome of Monte Carlo simulations of the Nitrogen-Vacancy coherence in presence of these dark spins matches experimental data suggesting the dark spins to be one of the main source of decoherence in scanning probe devices.
The first idea to recover coherence was to slow down the flipping rate of these dark spins by the means of the exchange bias effect. An antiferromagnet was deposited onto the diamond surface and in theory exchange interaction on the interface should pin the dark spins. In practice no detectable improvement in coherence time could be observed. It is an open question by how much pinning of decohering spins can improve the coherence of the NV-center and how complicated it is to pin only a few or single spins compared to a hole layer of magnetic spins. Further the finite thickness of the pinning layer increases the NV-sample distance leading to loss of sensitivity that needs to be balanced by the increase of coherence time. For these reasons an alternative route was pursued that does not recover coherence time but maintains the coherence time a priori by preventing the creation of dark spins. It is feasible that adhesion of the etching mask is of critical importance and that FOX does not provide sufficient adhesion to diamond. It is still unclear how the dark spins are produced but it is observed that bulk diamond shows almost

no DEER signal, pillars at the edge of a thin slab more and pillars in the middle of a thin slab the most DEER signal going along with a decrease in coherence time. We presented two methods to fabricate an etch mask made out of alumina which features a high etch resistivity and good adhesion to diamond. First measurements have shown a clear improvement in coherence time for NV-centers in diamond nanopillars. Still these results were not yet reproduced.
In the last chapter I introduced our effort into detecting spin labels on the surface. We succeeded in sensing a huge amount of spin labels but could not come up with positive results after dilution of spin labels. The next step would be to actively drive the spin labels and do DEER measurements on them.
Finally we tried to realize a theoretical idea, in which an amplifying electronic spins sits at the surface of diamond nano-crystals and senses the local magnetic environment with ultrahigh sensitivity. The electronic spin is then readout using an NV-center nearby. In our case the electronic spins were located at the end of the pillars with an NV-center 15 nm away. Unfortunately the spins tested did not fulfill necessary requirements to sense nuclear spins with it.

References

[1] Gopalakrishnan Balasubramanian, Philipp Neumann, Daniel Twitchen, Matthew Markham, Roman Kolesov, Norikazu Mizuochi, Junichi Isoya, Jocelyn Achard, Johannes Beck, Julia Tissler, et al. Ultralong spin coherence time in isotopically engineered diamond. *Nature materials*, 8(5):383–387, 2009.

[2] Iulia Buluta, Sahel Ashhab, and Franco Nori. Natural and artificial atoms for quantum computation. *Reports on Progress in Physics*, 74(10):104401, 2011.

[3] Ze-Liang Xiang, Sahel Ashhab, JQ You, and Franco Nori. Hybrid quantum circuits: Superconducting circuits interacting with other quantum systems. *Reviews of Modern Physics*, 85(2):623, 2013.

[4] Christian Kurtsiefer, Sonja Mayer, Patrick Zarda, and Harald Weinfurter. Stable solid-state source of single photons. *Physical Review Letters*, 85(2):290–293, 2000.

[5] G Kucsko, PC Maurer, NY Yao, M Kubo, HJ Noh, PK Lo, H Park, and MD Lukin. Nanometre-scale thermometry in a living cell. *Nature*, 500(7460):54–58, 2013.

[6] Florian Dolde, Helmut Fedder, Marcus W Doherty, Tobias Nöbauer, Florian Rempp, G Balasubramanian, T Wolf, F Reinhard, LCL Hollenberg, F Jelezko, et al. Electric-field sensing using single diamond spins. *Nature Physics*, 7(6):459–463, 2011.

[7] Y Martin and H Kumar Wickramasinghe. Magnetic imaging by force microscopy with 1000 å resolution. *Applied Physics Letters*, 50(20):1455–1457, 1987.

[8] AM Chang, HD Hallen, L Harriott, HF Hess, HL Kao, J Kwo, RE Miller, R Wolfe, J Van der Ziel, and TY Chang. Scanning hall probe microscopy. *Applied Physics Letters*, 61(16):1974–1976, 1992.

[9] JR Kirtley, MB Ketchen, KG Stawiasz, JZ Sun, WJ Gallagher, SH Blanton, and SJ Wind. High-resolution scanning squid microscope. *Applied Physics Letters*, 66(9):1138–1140, 1995.

[10] Thaddeus D Ladd, Fedor Jelezko, Raymond Laflamme, Yasunobu Nakamura, Christopher Monroe, and Jeremy L OBrien. Quantum computers. *Nature*, 464(7285):45–53, 2010.

[11] Patrick Maletinsky, Sungkun Hong, Michael Sean Grinolds, B Hausmann, Mikhail D Lukin, Ronald L Walsworth, Marko Loncar, and Amir Yacoby. A robust scanning diamond sensor for nanoscale imaging with single nitrogen-vacancy centres. *Nature nanotechnology*, 7(5):320–324, 2012.

[12] Marcus Schaffry, Erik M Gauger, John JL Morton, and Simon C Benjamin. Proposed spin amplification for magnetic sensors employing crystal defects. *Physical review letters*, 107(20):207210, 2011.

[13] Marcus W Doherty, Neil B Manson, Paul Delaney, Fedor Jelezko, Joerg Wrachtrup, and Lloyd CL Hollenberg. The nitrogen-vacancy colour centre in diamond. *Physics Reports*, 528(1):1–45, 2013.

[14] F Jelezko and J Wrachtrup. Single defect centres in diamond: A review. *physica status solidi (a)*, 203(13):3207–3225, 2006.

[15] Alexander Zaitsev. *Optical Properties of Diamond: A Data Handbook*. Springer Verlag, 2001.

[16] Hendrik Bluhm, Sandra Foletti, Izhar Neder, Mark Rudner, Diana Mahalu, Vladimir Umansky, and Amir Yacoby. Dephasing time of gaas electron-spin qubits coupled to a nuclear bath exceeding 200 [thinsp][mu] s. *Nature Physics*, 7(2):109–113, 2011.

[17] Andrew C Victor. Heat capacity of diamond at high temperatures. *The Journal of Chemical Physics*, 36(7):1903–1911, 2004.

[18] FP Bundy, HT Hall, HM Strong, and RH Wentorf. Man-made diamonds. *Nature*, 176(4471):51–55, 1955.

[19] Kenichi Ohno, F Joseph Heremans, Lee C Bassett, Bryan A Myers, David M Toyli, Ania C Bleszynski Jayich, Christopher J Palmstrøm, and David D Awschalom. Engineering shallow spins in diamond with nitrogen delta-doping. *Applied Physics Letters*, 101(8):082413, 2012.

[20] Linh My Pham, Nir Bar-Gill, Chinmay Belthangady, David Le Sage, Paola Cappellaro, MD Lukin, Amir Yacoby, and RL Walsworth. Enhanced solid-state multispin metrology using dynamical decoupling. *Physical Review B*, 86(4):045214, 2012.

[21] J Isoya, H Kanda, Y Uchida, SC Lawson, S Yamasaki, H Itoh, and Y Morita. Epr identification of the negatively charged vacancy in diamond. *Physical Review B*, 45:1436–1439, 1992.

[22] W Kaiser and WL Bond. Nitrogen, a major impurity in common type i diamond. *Physical review*, 115(4):857, 1959.

[23] A Gruber, A Dräbenstedt, C Tietz, L Fleury, J Wrachtrup, and C Von Borczyskowski. Scanning confocal optical microscopy and magnetic resonance on single defect centers. *Science*, 276(5321):2012–2014, 1997.

[24] AM Edmonds, UFS DHaenens-Johansson, RJ Cruddace, ME Newton, K-MC Fu, C Santori, RG Beausoleil, DJ Twitchen, and ML Markham. Production of oriented nitrogen-vacancy color centers in synthetic diamond. *Physical Review B*, 86(3):035201, 2012.

[25] Sebastien Pezzagna, Detlef Rogalla, Dominik Wildanger, Jan Meijer, and Alexander Zaitsev. Creation and nature of optical centres in diamond for single-photon emission - overview and critical remarks. *New Journal of Physics*, 13(3):035024, 2011.

[26] JR Maze, Adam Gali, Emre Togan, Yiwen Chu, Alexei Trifonov, Efthimios Kaxiras, and MD Lukin. Properties of nitrogen-vacancy centers in diamond: the group theoretic approach. *New Journal of Physics*, 13(2):025025, 2011.

[27] A Lenef and SC Rand. Electronic structure of the n-v center in diamond: Theory. *Physical Review B*, 53(20):13441, 1996.

[28] Jean Teissier, Arne Barfuss, Patrick Appel, Elke Neu, and P Maletinsky. Resolved sidebands in a strain-coupled hybrid spin-oscillator system. *arXiv preprint arXiv:1403.3405*, 2014.

[29] NB Manson, JP Harrison, and MJ Sellars. Nitrogen-vacancy center in diamond: Model of the electronic structure and associated dynamics. *Physical Review B*, 74(10):104303, 2006.

[30] Lucio Robledo, Hannes Bernien, Toeno van der Sar, and Ronald Hanson. Spin dynamics in the optical cycle of single nitrogen-vacancy centres in diamond. *New Journal of Physics*, 13(2):025013, 2011.

[31] Linh M. Pham. *Magnetic Field Sensing with Nitrogen-Vacancy Color Centers in Diamond*. PhD thesis, Harvard University, 2013.

[32] Nv diamond micro-magnetometer baseline studies. `http://www.dtic.mil/dtic/tr/fulltext/u2/a515818.pdf`. Accessed: 2014-01-13.

[33] A Dréau, M Lesik, L Rondin, P Spinicelli, O Arcizet, J-F Roch, and V Jacques. Avoiding power broadening in optically detected magnetic resonance of single nv defects for enhanced dc magnetic field sensitivity. *Physical Review B*, 84(19):195204, 2011.

[34] E. L. Hahn. Spin echoes. *Phys. Rev.*, 80:580–594, Nov 1950.

[35] JR Maze, PL Stanwix, JS Hodges, S Hong, JM Taylor, P Cappellaro, L Jiang, MV Gurudev Dutt, E Togan, AS Zibrov, et al. Nanoscale magnetic sensing with an individual electronic spin in diamond. *Nature*, 455(7213):644–647, 2008.

[36] L Childress, MV Gurudev Dutt, JM Taylor, AS Zibrov, F Jelezko, J Wrachtrup, PR Hemmer, and MD Lukin. Coherent dynamics of coupled electron and nuclear spin qubits in diamond. *Science*, 314(5797):281–285, 2006.

[37] D Le Sage, LM Pham, N Bar-Gill, C Belthangady, MD Lukin, A Yacoby, and RL Walsworth. Efficient photon detection from color centers in a diamond optical waveguide. *Physical Review B*, 85(12):121202, 2012.

[38] Alexios Beveratos, Sergei Kühn, Rosa Brouri, Thierry Gacoin, J-P Poizat, and Philippe Grangier. Room temperature stable single-photon source. *The European Physical Journal D-Atomic, Molecular, Optical and Plasma Physics*, 18(2):191–196, 2002.

[39] P Siyushev, F Kaiser, V Jacques, I Gerhardt, S Bischof, H Fedder, J Dodson, M Markham, D Twitchen, F Jelezko, et al. Monolithic diamond optics for single photon detection. *Applied physics letters*, 97(24):241902, 2010.

[40] Birgit JM Hausmann, Mughees Khan, Yinan Zhang, Tom M Babinec, Katie Martinick, Murray McCutcheon, Phil R Hemmer, and Marko Lončar. Fabrication of diamond nanowires for quantum information processing applications. *Diamond and Related Materials*, 19(5):621–629, 2010.

[41] Birgit JM Hausmann, Thomas M Babinec, Jennifer T Choy, Jonathan S Hodges, Sungkun Hong, Irfan Bulu, Amir Yacoby, Mikhail D Lukin, and Marko Lončar. Single-color centers implanted in diamond nanostructures. *New Journal of Physics*, 13(4):045004, 2011.

[42] M Lesik, J-P Tetienne, A Tallaire, J Achard, V Mille, A Gicquel, J-F Roch, and V Jacques. Perfect preferential orientation of nitrogen-vacancy defects in a synthetic diamond sample. *arXiv preprint arXiv:1401.2795*, 2014.

[43] Elke Neu, Patrick Appel, Marc Ganzhorn, Javier Miguel-Sánchez, Margarita Lesik, Vianney Mille, Vincent Jacques, Alexandre Tallaire, Jocelyn Achard, and Patrick Maletinsky. Photonic nano-structures on (111) oriented diamond. *Applied Physics Letters*, 104(15):153108, 2014.

[44] JM Taylor, P Cappellaro, L Childress, L Jiang, D Budker, PR Hemmer, A Yacoby, R Walsworth, and MD Lukin. High-sensitivity diamond magnetometer with nanoscale resolution. *Nature Physics*, 4(10):810–816, 2008.

[45] VM Acosta, E Bauch, MP Ledbetter, C Santori, K-MC Fu, PE Barclay, RG Beausoleil, H Linget, JF Roch, F Treussart, et al. Diamonds with a high density of nitrogen-vacancy centers for magnetometry applications. *Physical Review B*, 80(11):115202, 2009.

[46] Malcolm Levitt. *Spin Dynamics: Basics of Nuclear Magnetic Resonance*. Wiley-VCH Verlag, 2008.

[47] David M Toyli, Christoph D Weis, Gregory D Fuchs, Thomas Schenkel, and David D Awschalom. Chip-scale nanofabrication of single spins and spin arrays in diamond. *Nano letters*, 10(8):3168–3172, 2010.

[48] J. F. Ziegler. The stopping and range of ions in matter. `http://www.srim.org`. Accessed: 2013-11-22.

[49] Bryan A Myers, Matthieu C Dartiailh, Kenichi Ohno, Ananda Das, David D Awschalom, and Ania C Bleszynski Jayich. Probing surface noise with depth-calibrated spins in diamond. *arXiv preprint arXiv:1402.5392*, 2014.

[50] MS Grinolds, M Warner, K De Greve, Y Dovzhenko, L Thiel, RL Walsworth, S Hong, P Maletinsky, and A Yacoby. Sub-nanometer resolution in three-dimensional magnetic-resonance imaging of individual dark spins. *arXiv preprint arXiv:1401.2674*, 2014.

[51] Bernhard Grotz, Johannes Beck, Philipp Neumann, Boris Naydenov, Rolf Reuter, Friedemann Reinhard, Fedor Jelezko, Jörg Wrachtrup, David Schweinfurth, Biprajit Sarkar, et al. Sensing external spins with nitrogen-vacancy diamond. *New Journal of Physics*, 13(5):055004, 2011.

[52] HJ Mamin, MH Sherwood, and D Rugar. Detecting external electron spins using nitrogen-vacancy centers. *Physical Review B*, 86(19):195422, 2012.

[53] Gijs de Lange, Toeno van der Sar, Machiel Blok, Zhi-Hui Wang, Viatcheslav Dobrovitski, and Ronald Hanson. Controlling the quantum dynamics of a mesoscopic spin bath in diamond. *Scientific reports*, 2, 2012.

[54] Boris Naydenov, Friedemann Reinhard, Anke Laemmle, V Richter, Rafi Kalish, Ulrika FS DHaenens-Johansson, Mark Newton, Fedor Jelezko, and Joerg Wrachtrup. Increasing the coherence time of single electron spins in diamond by high temperature annealing. *Applied Physics Letters*, 97(24):242511, 2010.

[55] T Yamamoto, T Umeda, K Watanabe, S Onoda, ML Markham, DJ Twitchen, B Naydenov, LP McGuinness, T Teraji, S Koizumi, et al. Extending spin coherence times of diamond qubits by high-temperature annealing. *Physical Review B*, 88(7):075206, 2013.

[56] Yiwen Chu, Nathalie de Leon, Brendan Shields, Birgit JM Hausmann, Ruffin Evans, Emre Togan, Michael John Burek, Matthew Markham, Alastair Stacey, Alexander Zibrov, et al. Coherent optical transitions in implanted nitrogen vacancy centers. *Nano letters*, 2014.

[57] Grünberg Binasch, Peter Grünberg, F Saurenbach, and W Zinn. Enhanced magnetoresistance in layered magnetic structures with antiferromagnetic interlayer exchange. *Physical review B*, 39:4828–4830, 1989.

[58] Mario Norberto Baibich, JM Broto, Albert Fert, F Nguyen Van Dau, F Petroff, P Etienne, G Creuzet, A Friederich, and J Chazelas. Giant magnetoresistance of (001) fe/(001) cr magnetic superlattices. *Physical Review Letters*, 61(21):2472, 1988.

[59] J. M. D. Coey. *Magnetism and Magnetic Materials*. Cambridge University Press, 2010.

[60] William H Meiklejohn and Charles P Bean. New magnetic anisotropy. *Physical Review*, 105(3):904, 1957.

[61] X-rays unravel the puzzle of exchange bias. `http://www-ssrl.slac.stanford.edu/stohr/magneticexchange.htm`. Accessed: 2013-05-24.

[62] Iris Schmid. *The Role of Uncompensated Spins in Exchange Biased Systems*. PhD thesis, University of Basel, 2006.

[63] Michael Fraune, Ulrich Rüdiger, Gernot Güntherodt, Susana Cardoso, and Paulo Freitas. Size dependence of the exchange bias field in nio/ni nanostructures. *Applied Physics Letters*, 77(23):3815–3817, 2000.

[64] Sangsoo Noh, Eungahn Lee, Jeonghwan Seo, and Mehran Mehregany. Electrical properties of nickel oxide thin films for flow sensor application. *Sensors and Actuators A: Physical*, 125(2):363–366, 2006.

[65] HC Im, DC Choo, TW Kim, JH Kim, JH Seo, and YK Kim. Highly efficient organic light-emitting diodes fabricated utilizing nickel-oxide buffer layers between the anodes and the hole transport layers. *Thin Solid Films*, 515(12):5099–5102, 2007.

[66] T Gaebel, C Bradac, J Chen, JM Say, L Brown, P Hemmer, and JR Rabeau. Size-reduction of nanodiamonds via air oxidation. *Diamond and Related Materials*, 21:28–32, 2012.

[67] Hasan-Al Mehedi, Clément Hébert, Sébastien Ruffinatto, David Eon, Franck Omnès, and Etienne Gheeraert. Formation of oriented nanostructures in diamond using metallic nanoparticles. *Nanotechnology*, 23(45):455302, 2012.

[68] W Smirnov, JJ Hees, D Brink, W Müller-Sebert, A Kriele, OA Williams, and CE Nebel. Anisotropic etching of diamond by molten ni particles. *Applied Physics Letters*, 97(7):073117, 2010.

[69] N Edwin Widjonarko, Erin L Ratcliff, Craig L Perkins, Ajaya K Sigdel, Andriy Zakutayev, Paul F Ndione, Dane T Gillaspie, David S Ginley, Dana C Olson, and Joseph J Berry. Sputtered nickel oxide thin film for efficient hole transport layer in polymer–fullerene bulk-heterojunction organic solar cell. *Thin solid films*, 520(10):3813–3818, 2012.

[70] H Ohldag, A Scholl, F Nolting, E Arenholz, S Maat, AT Young, M Carey, and J Stöhr. Correlation between exchange bias and pinned interfacial spins. *Physical review letters*, 91(1):017203, 2003.

[71] Anoop Agrawal, Hamid R Habibi, Raj K Agrawal, John P Cronin, Dale M Roberts, R'Sue Caron-Popowich, and Carl M Lampert. Effect of deposition pressure on the microstructure and electrochromic properties of electron-beam-evaporated nickel oxide films. *Thin solid films*, 221(1):239–253, 1992.

[72] MS Grinolds, P Maletinsky, S Hong, MD Lukin, RL Walsworth, and A Yacoby. Quantum control of proximal spins using nanoscale magnetic resonance imaging. *Nature Physics*, 7(9):687–692, 2011.

[73] Michael J Burek, Nathalie P de Leon, Brendan J Shields, Birgit JM Hausmann, Yiwen Chu, Qimin Quan, Alexander S Zibrov, Hongkun Park, Mikhail D Lukin, and Marko Loncar. Free-standing mechanical and photonic nanostructures in single-crystal diamond. *Nano letters*, 12(12):6084–6089, 2012.

[74] HJ Mamin, M Kim, MH Sherwood, CT Rettner, K Ohno, DD Awschalom, and D Rugar. Nanoscale nuclear magnetic resonance with a nitrogen-vacancy spin sensor. *Science*, 339(6119):557–560, 2013.

[75] T Staudacher, F Shi, S Pezzagna, J Meijer, J Du, CA Meriles, F Reinhard, and J Wrachtrup. Nuclear magnetic resonance spectroscopy on a (5-nanometer) 3 sample volume. *Science*, 339(6119):561–563, 2013.

[76] MS Grinolds, S Hong, P Maletinsky, L Luan, MD Lukin, RL Walsworth, and A Yacoby. Nanoscale magnetic imaging of a single electron spin under ambient conditions. *Nature Physics*, 9(4):215–219, 2013.

A Dark spin simulation

The NV-spin-echo can easily be simulated assuming one knows the main decoherence source. In this case the decoherence source consists of statistically polarized dark spins with a phenomenological T1 time. This section explains the basic idea of a Monte Carlo simulator written by Mike Grinolds.
The Hahn-echo sequence on the NV is $\pi-\tau-\pi/2-\tau-\pi$ as described previously. In the simulation the evolution time τ is not continuous but has only a finite amount of points. For instance, if $\tau_{max} = 100$ us and npoints $= 5$, τ would be an array from 0 us to 100 with 5 points ([0 25 50 75 100]). For every point in the evolution time a linearly spaced vector that spans from 0 to the time of the point with a fixed number of bins is created. For instance, for the second point $\tau(2) = 25$ us and nbins $= 6$, the vector would be [0 5 10 15 20 25]. A dark spin configuration is associated to every bin in this vector. For simplicity we will assume only one dark spin. The spin state of the dark spin for the first bin will be given to be up. For every following bin the dark spins has a certain probability to flip. The number of spin flips for the whole vector [0 5 10 15 20 25] is given by a Poisson distribution. The mean parameter of this distribution is given by the duration of a time bin divided by T_1 of the dark spin. In this case the mean parameter would be 5 us$/T_1$. For now, we say this parameter is 3. So starting with a dark spin state up for the first bin, there have to happen three spin flips in the following bins, say at position 3,4 and 6.

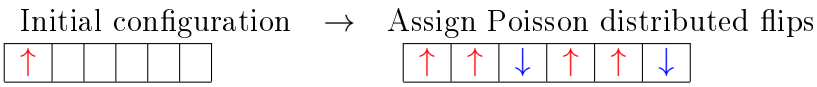

For each time bin the dipolar field produced by the electronic dark spin at the position of the NV and projected onto the NV-axis is calculated as

$$\vec{B}\left(\vec{r}\right) = \frac{\mu_o}{4\pi}\left(\frac{3\ \vec{r}\ (\vec{m}\cdot\vec{r})}{|\ \vec{r}\ |^5} - \frac{\vec{m}}{|\ \vec{r}\ |^3}\right) \tag{8}$$

with the vacuum permeability $\mu_o = 4\pi \cdot 10^{-7}\ Vs/Am$ and the magnetic moment of a dark spin $m = \mu_B = 9.274 \cdot 10^{-24}\ J/T$. For the spin configuration illustrated above this would yield a magnetic field at the NV as depicted in Fig. 36.

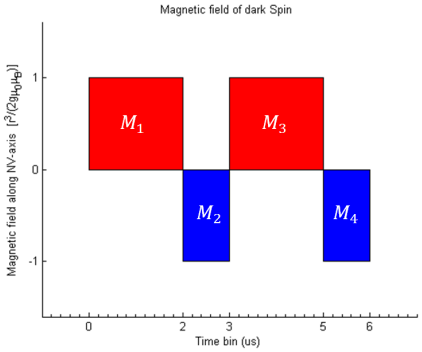

Figure 36: *Magnetic dipolar field magnitude of a dark spin at a distance r from the NV-center.*

A two-level system solver then calculates unitary rotation matrices for the field. For 3 spin flips, we will get 4 matrices. Let's say the amplitude of the magnetic field from the spin has 1 uT. The first matrix M_1 will give the rotation around the NV-axis for a field that is 1 uT and last for 2 us. M_2 will give the rotation around the NV-axis for a field that is -1 uT and last for 1 us. M_3 will give the rotation around the NV-axis for a field that is 1 uT and last for 2 us. M_4 will give the rotation around the NV-axis for a field that is -1 uT and last for 1 us. The NV-state after the sequence is then simply

$$|NV\rangle = U_{\pi/2} \otimes M_4 \otimes M_3 \otimes U_\pi \otimes M_2 \otimes M_1 \otimes U_{\pi/2} \otimes \begin{pmatrix} 1 \\ 0 \end{pmatrix} \tag{9}$$

where U_π and $U_{\pi/2}$ are the unitary matrices for the π and $\pi/2$-pulse, respectively. The initial state of the NV is assumed to be up.
This way, the NV-state is calculated for each point of evolution [0 25 50 75 100] to give the final coherence curve as shown in Fig. 16.